The Sloan Lens ACS Survey

Auger, M. W.; Treu, T.; Bolton, A. S.; Gavazzi, R.; Koopmans, L. V. E.; Marshall, P. J.; Moustakas, L. A.; Burles, S.

Published in:
Astrophysical Journal

DOI:
10.1088/0004-637X/724/1/511

Publication date:
2010

The Astrophysical Journal, 724:511–525, 2010 November 20 doi:10.1088/0004-637X/724/1/511

THE SLOAN LENS ACS SURVEY. X. STELLAR, DYNAMICAL, AND TOTAL MASS CORRELATIONS OF MASSIVE EARLY-TYPE GALAXIES

M. W. Auger[1], T. Treu[1,8], A. S. Bolton[2], R. Gavazzi[3], L. V. E. Koopmans[4], P. J. Marshall[1,5], L. A. Moustakas[6], and S. Burles[7]

[1] Department of Physics, University of California, Santa Barbara, CA 93106, USA; mauger@physics.ucsb.edu
[2] Department of Physics and Astronomy, University of Utah, Salt Lake City, UT 84112, USA
[3] Institut d'Astrophysique de Paris, UMR7095 CNRS & Univ. Pierre et Marie Curie, 98bis Bvd Arago, F-75014 Paris, France
[4] Kapteyn Astronomical Institute, University of Groningen, P.O. Box 800, 9700AV Groningen, The Netherlands
[5] Kavli Institute for Particle Astrophysics and Cosmology, Stanford University, Stanford, CA 94305, USA
[6] Jet Propulsion Laboratory, California Institute of Technology, 4800 Oak Grove Drive, M/S 169-237, Pasadena, CA 91109, USA
[7] D. E. Shaw & Co., L.P., 20400 Stevens Creek Boulevard, Suite 850, Cupertino, CA 95014, USA
Received 2010 June 8; accepted 2010 September 17; published 2010 November 3

ABSTRACT

We use stellar masses, surface photometry, strong-lensing masses, and stellar velocity dispersions ($\sigma_{e/2}$) to investigate empirical correlations for the definitive sample of 73 early-type galaxies (ETGs) that are strong gravitational lenses from the SLACS survey. The traditional correlations (fundamental plane (FP) and its projections) are consistent with those found for non-lens galaxies, supporting the thesis that SLACS lens galaxies are representative of massive ETGs (dimensional mass $M_{\rm dim} = 10^{11}$–$10^{12}\ M_{\odot}$). The addition of high-precision strong-lensing estimates of the total mass allows us to gain further insights into their internal structure: (1) the average slope of the total mass-density profile ($\rho_{\rm tot} \propto r^{-\gamma'}$) is $\langle\gamma'\rangle = 2.078 \pm 0.027$ with an intrinsic scatter of 0.16 ± 0.02; (2) γ' correlates with effective radius (r_e) and central mass density, in the sense that denser galaxies have steeper profiles; (3) the dark matter (DM) fraction within $r_e/2$ is a monotonically increasing function of galaxy mass and size (due to a mass-dependent central cold DM distribution or due to baryonic DM—stellar remnants or low-mass stars—if the initial mass function is non-universal and its normalization increases with mass); (4) the dimensional mass $M_{\rm dim} \equiv 5 r_e \sigma^2_{e/2}/G$ is proportional to the total (lensing) mass $M_{r_e/2}$, and both increase more rapidly than stellar mass M_* ($M_* \propto M^{0.8}_{r_e/2}$); (5) the mass plane (MP), obtained by replacing surface brightness with surface mass density in the FP, is found to be tighter and closer to the virial relation than the FP and the M_*P, indicating that the scatter of those relations is dominated by stellar population effects; (6) we construct the fundamental hyper-plane by adding stellar masses to the MP and find the M_* coefficient to be consistent with zero and no residual intrinsic scatter. Our results demonstrate that the dynamical structure of ETGs is not scale invariant and that it is fully specified by $M_{r_e/2}$, r_e, and $\sigma_{e/2}$. Although the basic trends can be explained qualitatively in terms of varying star formation efficiency as a function of halo mass and as the result of dry and wet mergers, reproducing quantitatively the observed correlations and their tightness may be a significant challenge for galaxy formation models.

Key words: dark matter – galaxies: elliptical and lenticular, cD – galaxies: fundamental parameters – galaxies: structure – gravitational lensing: strong

Online-only material: color figures

1. INTRODUCTION

The hierarchical model for structure formation in the context of a cold dark matter cosmology (ΛCDM) has been tremendously successful at describing the large-scale features of the universe (e.g., Komatsu et al. 2009). However, there are many important properties of the universe at galactic and sub-galactic scales that have evaded detailed understanding. For example, the several bi-modal classes of galaxies (e.g., red/blue color, early/late-type morphology; Balogh et al. 2004), the so-called downsizing of star formation (Cowie et al. 1996; Cooper et al. 2006; Bundy et al. 2006), the tight empirical correlations between the observed properties of early-type galaxies (ETGs; Faber & Jackson 1976; Kormendy 1977; Dressler et al. 1987; Djorgovski & Davis 1987), correlations (or the lack of correlations) between these and the local density (Dressler 1980; Cooper et al. 2006), and the absence of local analogs to extremely compact high-redshift galaxies (Daddi et al. 2005; Trujillo et al. 2006; van Dokkum et al. 2008).

One important step in understanding these phenomena is to explore the relationship between the baryonic matter that dominates astrophysical observables and the dark matter (DM) that is postulated in the ΛCDM model. High-precision measurements at galaxy scales are essential to test whether apparent inconsistencies between the observed universe and DM only cosmological simulations can be reconciled by an improved understanding of the detailed physical mechanisms governing baryons and their interaction with DM, or whether a rethinking of the CDM paradigm might be necessary. Within this context, the origin of ETGs is currently a point of discord between observation and theory, and therefore its investigation carries enormous potential for discovery. Although their formation via merging of spiral disks is one of the assumptions of the standard paradigm, it remains to be seen whether this can work in detail.

The tight empirical correlations between the observed properties of ETGs are a powerful phenomenological tool to relate baryonic and DM. Among these, the correlation between size, surface brightness, and stellar velocity dispersion known as the fundamental plane (hereafter FP; Faber et al. 1987; Djorgovski & Davis 1987), and its mass counterpart the stellar mass plane

[8] Packard Fellow.

(M_*P, where surface brightness is replaced by stellar mass; e.g., Hyde & Bernardi 2009b) have provided two key insights. First, the correlations are "tilted" in the sense that they cannot be explained by assuming that ETGs are a self-similar family, they obey the virial theorem, and have a constant mass-to-light ratio (Faber et al. 1987; Ciotti et al. 1996); mounting evidence, including the alignment of the mass plane (MP; Bolton et al. 2007) with the virial plane, suggests that the dominant cause of the tilt is a mass-dependent central DM fraction (e.g., Bolton et al. 2008b; Tortora et al. 2009). Second, the correlations are remarkably tight (Jorgensen et al. 1996; Hyde & Bernardi 2009b; Graves & Faber 2010) implying that for a given size and velocity dispersion there is very little scatter in the star formation histories of ETGs. Previous studies have found a slight misalignment between the FP and M_*P (Hyde & Bernardi 2009b) which likely results from constructing the FP with galaxies that span a variety of ages, since age correlates with both stellar mass (more massive galaxies form earlier) and the stellar mass-to-light ratio (older stellar populations have larger stellar M/L for a given stellar mass).

Additional progress in understanding ETGs has been made by attempting to infer the separate luminous and dark components in the central regions of galaxies. Tortora et al. (2009) use dynamical masses determined from central velocity dispersion measurements with stellar masses inferred from stellar populations synthesis (SPS) models to obtain the central DM fraction; they find a clear dependence on total mass in the sense that more massive galaxies have larger DM fractions (also see Napolitano et al. 2010), although they assume a mass-traces-light distribution or a singular isothermal sphere mass distribution. The assumption of an isothermal central mass profile seems to be robust, as illustrated by modeling of X-ray data (Humphrey & Buote 2010) and strong lensing and stellar kinematics (Koopmans et al. 2006, 2009; Barnabè et al. 2009; Barnabe et al. 2010), although the origin of this isothermality remains unclear.

We use a sample of early-type gravitational lenses from the Sloan Lens ACS Survey (SLACS; Bolton et al. 2006, 2008a; Auger et al. 2009) to investigate the scaling relations of ETGs, and in particular we look at the relationships between total and stellar mass with respect to the other structural parameters of lenses. We exploit multiple lines of observation—including strong lensing, stellar dynamics, and SPS models—to distinguish between the luminous and dark mass, and we construct the FP, M_*P, and MP for the SLACS ETGs. The paper is organized as follows. In Section 2, we present the SLACS data set, summarize observables listed in previous papers and used for this analysis, and present new quantities, such as improved estimates for the total mass within half of the effective radius and the central slope of the total mass-density profile. Section 3 describes bivariate empirical correlations derived for the SLACS sample, starting from traditional ones including non-lensing observables and concluding with those including total mass as derived from strong lensing. Section 4 describes correlations in higher dimensions, including the FP, M_*P, MP, and the newly derived fundamental hyper-plane (FPH). Section 5 discusses our results and Section 6 gives a brief summary. A standard cosmological model with $\Omega_m = 0.3$, $\Omega_\Lambda = 0.7$, and $h = 0.7$ is assumed throughout.

2. THE SLACS SURVEY DATA: OBSERVABLES AND DERIVED QUANTITIES

There are 85 confirmed (grade "A") strong gravitational lenses that have been discovered by SLACS (Bolton et al. 2008a; Auger et al. 2009). These include 73 galaxies with E or S0 morphologies which we take to be the ETGs from SLACS and which we focus on in this paper. A wealth of data exists for each of these galaxies, including high-resolution multi-band optical and near-infrared *Hubble Space Telescope* (*HST*) imaging and fiber-based optical spectroscopy from the Sloan Digital Sky Survey (SDSS; York et al. 2000). These data are used to infer several fundamental properties of the lenses, which we briefly detail below and list in Table 1. Some of the observables and derived quantities have been given in previous papers of the SLACS series, and will not be repeated in Table 1 for conciseness. The present compilation is based on the most up-to-date data and calibrations and supercedes the information presented in previous papers.

2.1. Stellar Masses, Luminosities, and Effective Radii

The high-resolution multi-band *HST* imaging is used to infer stellar masses M_* for each system (Auger et al. 2009) using SPS models and assuming either a Chabrier or Salpeter initial mass function (IMF). Four systems only have one band of *HST* imaging and we exclude these from our analysis when stellar masses are required. The SPS models provide robust synthetic photometry (sometimes referred to as k-corrections, or k-color corrections) that is approximately insensitive to the assumed IMF and these models therefore yield accurate estimates for the B- and V-band rest-frame luminosity. The same models also allow us to compute rest-frame luminosities of each galaxy passively evolved to $z = 0$ in a self-consistent manner; B- and V-band luminosities at the redshift of the lens and corrected to $z = 0$ can be found in Auger et al. (2009).

Furthermore, we use the *HST* imaging to determine the effective radius in each band, and we employ a linear model of effective radius as a function of wavelength to infer the rest-frame V-band effective radius. We assume $r_{e,\lambda} = a * \lambda + b$ where a and b are determined from a fit to the observations of r_e in each filter with rest-frame wavelength given by $\lambda_c/(1+z)$ where λ_c is the filter central wavelength (e.g., Treu et al. 2001). Then $r_{e,5500}$ is the effective radius used throughout this paper. As discussed by Bolton et al. (2008b), our assumption of de Vaucouleurs (1948) profiles is valid in the luminosity range covered by the SLACS sample. The systematic trends in Sérsic index n (Sérsic 1968) for such high-luminosity galaxies are dominated by the intrinsic scatter in the correlation. As expected, by fitting the SLACS lenses with Sérsic models, we find no correlation between n and any of the global galactic quantities. Likewise the adoption of Sérsic profiles does not change any of the trends presented here. Therefore, we limit our analysis to the simpler and better constrained de Vaucouleurs models. This does not affect our interpretation of the tilt of the FP and other key structural parameters, as the effect of varying n is negligible in the probed mass range (Nipoti et al. 2008).

2.2. Stellar Velocity Dispersions and Dynamical Masses

The SDSS spectroscopy provides an estimate of the luminosity-weighted stellar velocity dispersion within the 3″ diameter aperture of the SDSS fibers which we refer to as σ_{SDSS}. We use the prescription of Jorgensen et al. (1995) to infer the velocity dispersion within half of the effective radius, $\sigma_{e/2}$, for our analysis of the scaling relations and parameter planes but use the aperture velocity dispersion in our analysis of the central mass profile (Section 3.3).

Table 1
Mass and Structural Parameters for SLACS Early-type Lenses

Lens Name	$r_{e,V}$	$\sigma_{e/2}$	$\log(M_*/M_\odot)$		$\log(M_{r_e/2}/M_\odot)$	$f_{\rm DM}$		γ'
	(kpc)	(km s^{-1})	Chab	Salp		Chab	Salp	
SDSSJ0029−0055†	8.36	231 ± 18	11.33 ± 0.13	11.58 ± 0.13	11.13 ± 0.03	0.47 ± 0.15	0.04 ± 0.28	2.38 ± 0.23
SDSSJ0037−0942	7.44	282 ± 10	11.48 ± 0.06	11.73 ± 0.06	11.36 ± 0.02	0.57 ± 0.07	0.25 ± 0.11	2.14 ± 0.07
SDSSJ0044+0113	6.12	267 ± 13	11.23 ± 0.09	11.47 ± 0.09	11.13 ± 0.07	0.59 ± 0.10	0.29 ± 0.18	2.31 ± 0.24
SDSSJ0216−0813	13.19	334 ± 23	11.79 ± 0.07	12.03 ± 0.07	11.76 ± 0.02	0.65 ± 0.06	0.40 ± 0.11	2.09 ± 0.20
SDSSJ0252+0039	5.68	170 ± 12	11.21 ± 0.13	11.46 ± 0.13	10.97 ± 0.03	0.42 ± 0.18	−0.03 ± 0.32	1.57 ± 0.12
SDSSJ0330−0020	6.23	220 ± 21	11.35 ± 0.09	11.58 ± 0.09	11.14 ± 0.05	0.46 ± 0.12	0.09 ± 0.21	1.91 ± 0.18
SDSSJ0728+3835	5.86	219 ± 11	11.44 ± 0.12	11.69 ± 0.12	11.12 ± 0.02	0.31 ± 0.19	−0.23 ± 0.37	1.86 ± 0.10
SDSSJ0737+3216†	14.10	338 ± 16	11.72 ± 0.07	11.96 ± 0.07	11.52 ± 0.03	0.49 ± 0.09	0.10 ± 0.16	2.68 ± 0.12
SDSSJ0819+4534†	7.63	227 ± 15	11.15 ± 0.08	11.40 ± 0.08	11.16 ± 0.04	0.68 ± 0.07	0.43 ± 0.12	2.16 ± 0.25
SDSSJ0822+2652	7.64	263 ± 15	11.43 ± 0.13	11.69 ± 0.13	11.32 ± 0.02	0.56 ± 0.13	0.21 ± 0.23	2.12 ± 0.14
SDSSJ0912+0029	11.69	322 ± 12	11.71 ± 0.07	11.96 ± 0.07	11.71 ± 0.02	0.67 ± 0.06	0.43 ± 0.09	1.98 ± 0.09
SDSSJ0935−0003†	20.09	391 ± 35	11.72 ± 0.07	11.96 ± 0.07	11.81 ± 0.14	0.73 ± 0.09	0.53 ± 0.15	2.44 ± 0.36
SDSSJ0936+0913	7.00	246 ± 11	11.43 ± 0.12	11.68 ± 0.12	11.18 ± 0.02	0.40 ± 0.17	−0.07 ± 0.30	2.24 ± 0.12
SDSSJ0946+1006	9.08	265 ± 21	11.34 ± 0.12	11.59 ± 0.12	11.43 ± 0.02	0.73 ± 0.07	0.51 ± 0.14	2.01 ± 0.18
SDSSJ0956+5100	8.58	338 ± 15	11.56 ± 0.09	11.81 ± 0.08	11.52 ± 0.02	0.64 ± 0.07	0.36 ± 0.13	2.30 ± 0.09
SDSSJ0959+0410	3.34	203 ± 13	10.91 ± 0.07	11.15 ± 0.06	10.76 ± 0.02	0.54 ± 0.08	0.20 ± 0.13	2.05 ± 0.15
SDSSJ0959+4416	7.27	248 ± 19	11.47 ± 0.12	11.72 ± 0.12	11.23 ± 0.02	0.42 ± 0.17	−0.03 ± 0.30	2.14 ± 0.21
SDSSJ1016+3859	4.38	254 ± 13	11.23 ± 0.12	11.48 ± 0.12	11.04 ± 0.02	0.48 ± 0.15	0.08 ± 0.26	2.19 ± 0.11
SDSSJ1020+1122	6.23	290 ± 18	11.54 ± 0.12	11.80 ± 0.12	11.34 ± 0.03	0.46 ± 0.16	0.04 ± 0.28	2.08 ± 0.12
SDSSJ1023+4230	5.97	247 ± 15	11.33 ± 0.12	11.57 ± 0.12	11.19 ± 0.03	0.55 ± 0.13	0.20 ± 0.23	2.01 ± 0.11
SDSSJ1029+0420	3.02	215 ± 9	11.04 ± 0.12	11.29 ± 0.11	10.71 ± 0.02	0.28 ± 0.19	−0.28 ± 0.34	2.28 ± 0.10
SDSSJ1106+5228	3.61	266 ± 9	11.13 ± 0.06	11.37 ± 0.06	10.91 ± 0.02	0.47 ± 0.08	0.07 ± 0.13	2.40 ± 0.07
SDSSJ1112+0826	6.48	328 ± 20	11.48 ± 0.09	11.73 ± 0.08	11.43 ± 0.03	0.63 ± 0.08	0.34 ± 0.13	2.21 ± 0.10
SDSSJ1134+6027	5.26	243 ± 11	11.26 ± 0.12	11.51 ± 0.12	11.06 ± 0.02	0.48 ± 0.14	0.06 ± 0.25	2.20 ± 0.11
SDSSJ1142+1001	6.99	225 ± 22	11.30 ± 0.08	11.55 ± 0.08	11.22 ± 0.02	0.60 ± 0.08	0.31 ± 0.13	1.90 ± 0.23
SDSSJ1143−0144	10.25	263 ± 5	11.36 ± 0.09	11.60 ± 0.09	11.50 ± 0.03	0.77 ± 0.05	0.59 ± 0.09	1.92 ± 0.06
SDSSJ1153+4612	4.00	233 ± 15	11.08 ± 0.13	11.33 ± 0.13	10.90 ± 0.03	0.50 ± 0.14	0.10 ± 0.26	2.28 ± 0.13
SDSSJ1204+0358	4.59	274 ± 17	11.20 ± 0.07	11.45 ± 0.06	11.09 ± 0.03	0.58 ± 0.07	0.26 ± 0.12	2.29 ± 0.11
SDSSJ1205+4910	9.04	282 ± 13	11.48 ± 0.06	11.72 ± 0.06	11.42 ± 0.02	0.63 ± 0.06	0.36 ± 0.10	2.16 ± 0.12
SDSSJ1213+6708†	6.51	292 ± 11	11.24 ± 0.10	11.49 ± 0.09	11.17 ± 0.02	0.61 ± 0.08	0.31 ± 0.14	2.49 ± 0.08
SDSSJ1218+0830	7.62	218 ± 10	11.35 ± 0.08	11.59 ± 0.08	11.26 ± 0.02	0.60 ± 0.08	0.30 ± 0.13	1.82 ± 0.11
SDSSJ1250+0523	6.88	256 ± 14	11.53 ± 0.07	11.77 ± 0.07	11.20 ± 0.02	0.31 ± 0.11	−0.22 ± 0.20	2.30 ± 0.12
SDSSJ1306+0600	6.12	241 ± 17	11.19 ± 0.08	11.43 ± 0.08	11.22 ± 0.02	0.70 ± 0.06	0.47 ± 0.10	1.89 ± 0.14
SDSSJ1313 + 4615	6.51	266 ± 18	11.33 ± 0.09	11.58 ± 0.08	11.27 ± 0.02	0.63 ± 0.08	0.34 ± 0.12	2.06 ± 0.14
SDSSJ1318−0313	14.05	211 ± 18	11.43 ± 0.09	11.67 ± 0.09	11.60 ± 0.02	0.78 ± 0.04	0.61 ± 0.08	1.64 ± 0.15
SDSSJ1330−0148	1.39	194 ± 9	10.43 ± 0.06	10.67 ± 0.06	10.31 ± 0.03	0.57 ± 0.07	0.26 ± 0.12	2.25 ± 0.10
SDSSJ1402 + 6321	8.92	268 ± 17	11.55 ± 0.07	11.79 ± 0.06	11.45 ± 0.02	0.59 ± 0.07	0.28 ± 0.11	1.97 ± 0.14
SDSSJ1403 + 0006	5.10	218 ± 17	11.20 ± 0.08	11.44 ± 0.08	10.97 ± 0.02	0.45 ± 0.11	0.04 ± 0.19	2.14 ± 0.23
SDSSJ1416 + 5136	5.92	248 ± 25	11.40 ± 0.08	11.64 ± 0.08	11.22 ± 0.05	0.50 ± 0.11	0.12 ± 0.20	1.90 ± 0.16
SDSSJ1420 + 6019	2.56	208 ± 4	10.93 ± 0.06	11.17 ± 0.06	10.59 ± 0.02	0.30 ± 0.10	−0.23 ± 0.18	2.28 ± 0.07
SDSSJ1430 + 4105	10.41	325 ± 32	11.68 ± 0.12	11.93 ± 0.11	11.64 ± 0.02	0.63 ± 0.10	0.35 ± 0.18	2.06 ± 0.18
SDSSJ1436−0000	10.34	226 ± 17	11.45 ± 0.08	11.69 ± 0.09	11.39 ± 0.02	0.63 ± 0.07	0.35 ± 0.13	1.88 ± 0.19
SDSSJ1443 + 0304	2.64	218 ± 11	10.87 ± 0.06	11.12 ± 0.06	10.67 ± 0.02	0.49 ± 0.08	0.09 ± 0.14	2.31 ± 0.12
SDSSJ1451−0239	5.83	224 ± 14	11.17 ± 0.07	11.39 ± 0.06	11.00 ± 0.03	0.52 ± 0.08	0.19 ± 0.13	2.24 ± 0.19
SDSSJ1525 + 3327	14.13	265 ± 26	11.78 ± 0.09	12.02 ± 0.09	11.72 ± 0.02	0.63 ± 0.08	0.35 ± 0.14	1.77 ± 0.20
SDSSJ1531−0105	7.54	280 ± 12	11.43 ± 0.09	11.68 ± 0.09	11.35 ± 0.02	0.61 ± 0.08	0.30 ± 0.14	2.13 ± 0.08
SDSSJ1538 + 5817	3.63	194 ± 12	11.03 ± 0.08	11.28 ± 0.08	10.80 ± 0.03	0.45 ± 0.10	0.02 ± 0.18	1.90 ± 0.14
SDSSJ1614 + 4522†	8.18	183 ± 13	11.21 ± 0.13	11.47 ± 0.12	11.07 ± 0.06	0.54 ± 0.16	0.15 ± 0.27	2.00 ± 0.29
SDSSJ1621 + 3931	8.85	239 ± 20	11.45 ± 0.06	11.70 ± 0.07	11.41 ± 0.02	0.64 ± 0.06	0.36 ± 0.10	1.80 ± 0.16
SDSSJ1627−0053	6.87	295 ± 14	11.45 ± 0.09	11.70 ± 0.09	11.30 ± 0.02	0.54 ± 0.10	0.19 ± 0.17	2.33 ± 0.10
SDSSJ1630 + 4520	7.80	281 ± 16	11.61 ± 0.07	11.86 ± 0.07	11.43 ± 0.03	0.50 ± 0.09	0.13 ± 0.15	1.97 ± 0.09
SDSSJ1636 + 4707	5.93	237 ± 15	11.38 ± 0.08	11.63 ± 0.08	11.13 ± 0.02	0.42 ± 0.12	−0.04 ± 0.21	2.09 ± 0.14
SDSSJ1644 + 2625	4.49	234 ± 12	11.18 ± 0.09	11.43 ± 0.08	11.00 ± 0.02	0.50 ± 0.10	0.12 ± 0.16	2.09 ± 0.10
SDSSJ1719 + 2939	4.32	295 ± 15	11.22 ± 0.08	11.46 ± 0.08	11.12 ± 0.02	0.59 ± 0.08	0.28 ± 0.14	2.36 ± 0.09
SDSSJ2238−0754	5.78	200 ± 11	11.20 ± 0.06	11.45 ± 0.06	11.07 ± 0.02	0.57 ± 0.07	0.23 ± 0.12	1.79 ± 0.12
SDSSJ2300 + 0022	6.88	284 ± 17	11.40 ± 0.07	11.65 ± 0.07	11.36 ± 0.02	0.64 ± 0.06	0.37 ± 0.10	2.06 ± 0.13
SDSSJ2303 + 1422	9.30	253 ± 16	11.47 ± 0.06	11.71 ± 0.06	11.46 ± 0.02	0.67 ± 0.05	0.42 ± 0.09	1.86 ± 0.13
SDSSJ2321−0939	6.52	246 ± 8	11.35 ± 0.08	11.60 ± 0.08	11.20 ± 0.02	0.54 ± 0.09	0.19 ± 0.16	2.02 ± 0.08
SDSSJ2341 + 0000	10.59	206 ± 13	11.48 ± 0.08	11.73 ± 0.08	11.45 ± 0.02	0.65 ± 0.07	0.38 ± 0.12	1.62 ± 0.12

Notes. Columns: (1) lens name; (2) effective radius, corrected to the rest-frame *V*-band, in kpc; (3) central velocity dispersion within half of the effective radius; (4 and 5) total stellar mass assuming a Chabrier (Column 4) or Salpeter (Column 5) IMF; (6) total mass within half of the effective radius, as determined from our power-law mass distribution models; (7 and 8) dark matter fraction within half of the effective radius for Chabrier and Salpeter IMFs; and (9) slope of the power-law mass distribution, $\rho \propto r^{-\gamma}$.

We combine effective radii and stellar velocity dispersions to construct a dimensional mass, defined as

$$M_{\rm dim} \equiv \frac{5 r_e \sigma_{e/2}^2}{G}, \quad (1)$$

where the number 5 is the canonical choice for the virial coefficient of dynamical masses of massive ETGs (e.g., Bernardi et al. 2003; Cappellari et al. 2006). We note that the dimensional mass is not actually the dynamical mass (e.g., Bolton et al. 2008b), but we choose this form to simplify comparison with dynamical masses.

2.3. Einstein Radii, Mass-density Profile Slopes, and Strong-lensing Masses

Singular isothermal ellipsoid (SIE) lens model fits to the *HST* data have been used to derive Einstein radii for each lens systems (Bolton et al. 2008a; Auger et al. 2009). The lens and source redshifts are known from the SDSS spectroscopy, and we can therefore infer the SIE velocity dispersion, which we refer to as $\sigma_{\rm SIE}$ (e.g., Bolton et al. 2008a). Our SIE mass models also robustly constrain the total projected mass within the Einstein radii to a precision of a few percent (Bolton et al. 2008a).

We use the available information to constrain power-law total mass distribution models for each lensing galaxy. The mass distributions are defined as in Treu & Koopmans (2004) and Koopmans et al. (2006, 2009), with $\rho \propto r^{-\gamma'}$, and these models are constrained using the mass within the Einstein radius, the SDSS stellar velocity dispersion, and de Vaucouleurs fits to the stellar light distribution. Details of how the fits are implemented can be found in Suyu et al. (2010; see also Koopmans et al. 2006, 2009), although for this analysis we only use our baseline models, characterized by a Hernquist (1990) model for the stellar distribution and no anisotropy of the stellar orbits. The isotropy assumption is consistent with complementary (e.g., Treu & Koopmans 2004; Koopmans et al. 2009) and more detailed (e.g., Barnabè et al. 2009) investigations of the SLACS lenses. Note, however, that while mild radial anisotropy would lead to a slightly shallower inferred mass slope (e.g., Koopmans et al. 2009), it would cause the inference on the mass within a central aperture to be over- or underestimated, depending on whether the aperture is smaller or larger than the Einstein radius. We list the updated mass slopes γ' for all lenses with robust kinematic and lensing data in Table 1; this extends and completes our analysis of power-law mass models for the SLACS lenses based upon the SDSS spectroscopy (e.g., Koopmans et al. 2006, 2009). We use these power-law models to infer the total projected mass within half of the effective radius (denoted $M_{r_e/2}$; this radius is chosen because it is well matched to the typical Einstein radius and therefore leads to the smallest errors from extrapolating the power-law mass model) which is used in our analysis of the scaling relations and parameter planes of the lens galaxies.

2.4. Mass-to-Light Ratios and Dark Matter Fractions

We construct three different estimators of the central mass-to-light ratio, by computing the ratio between total (lensing) mass, dimensional, and stellar mass and luminosity within $r_e/2$. The three ratios are referred to as the total mass-to-light ratio (or $M_{r_e/2}/L$), the dimensional mass-to-light ratio ($M_{\rm dim}/L$) and the stellar mass-to-light ratio (M_*/L). When needed, we use the symbol M/L to refer to the three mass-to-light ratios collectively.

The mass-to-light ratio is relevant for understanding observations but simulations are more readily understood in the context of dark (or stellar) mass fraction. We use the stellar masses derived from SPS models (Auger et al. 2009) in conjunction with the total mass within half of the effective radius determined from lensing and dynamics to infer the *projected* (i.e., within a cylinder) DM fraction, $f_{\rm DM} = 1 - M_*/M_{r_e/2}$ where M_* has been scaled to the stellar mass within $r_e/2$ (this is 32% of the total stellar mass for a de Vaucouleurs distribution) and any gas is effectively treated as DM. We note that the projected DM fraction is always larger than the (three-dimensional) DM fraction within a sphere of equal radius because of the contribution of the outer parts of the halo to the projected quantity. We adopt in this paper the projected (two-dimensional) DM fraction because it is the most robustly determined quantity and the one closest to the observables. However, the interested reader can derive the three-dimensional DM fraction from the projected fraction using the effective radii and mass-density profile slopes given in Table 1.

3. BIVARIATE CORRELATIONS

Bivariate empirical correlations between properties of ETGs, e.g., the L–σ (Faber & Jackson 1976) and L–r_e (Kormendy 1977) relations, are extremely useful for a number of practical applications, including modeling of complex data and simulations of mock catalogs. Although ETGs are known to be at least a two parameter family, the bivariate correlations encode critical information about the distribution of ETGs in higher-dimensional parameter spaces and therefore can be used to provide additional tests of theoretical models. For example, although dry mergers generally move ETGs inside the FP, they also tend to move galaxies away from its two-dimensional projections (Nipoti et al. 2003; Boylan-Kolchin et al. 2006).

We fit several bivariate empirical correlations to the SLACS data described in Section 2. We have determined linear fits to each correlation (these correlations are frequently between the logarithm of physical quantities and a linear fit therefore represents a power-law model) that account for the errors in both the dependent and independent variables as well as covariance between the measurement errors, and we also explicitly determine the intrinsic scatter. We use a Python implementation of the fitting technique proposed by Kelly (2007), which uses a Bayesian framework to avoid biases introduced by inappropriate choices for the prior distributions of the independent variables; we have found that this is particularly important when the errors on the independent variables are significantly larger than the errors on the dependent variables.

We have restricted our analysis of these correlations to the early-type lenses, which we assume share similar formation and evolution histories. However, Jiang & Kochanek (2007) suggest that the SLACS lenses are either not an homologous population or the stellar velocity dispersions have significantly underestimated systematic errors (e.g., Hyde & Bernardi 2009a, who show that different velocity dispersion codes produce systematically different results). We find that six galaxies in our sample are significant outliers of the hyper-plane relation between size, velocity dispersion, stellar mass, and total mass given by Equation (3) (these systems are indicated in Table 1). We have investigated the nature of these outliers but find that they generally do not stand out from the other lensing galaxies; none of these discrepant objects have disky structure, nor do they have anomalous spectral features. Furthermore, we have determined the stellar velocity dispersions for each

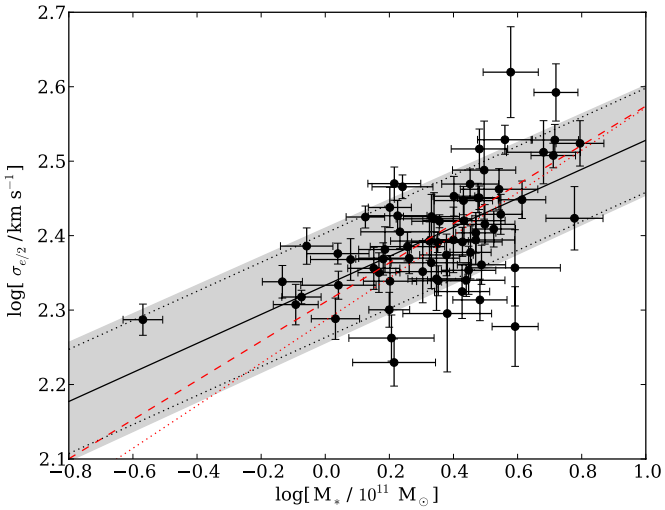

Figure 1. $\sigma_{e/2}$–M_* relation for SLACS lenses. The solid black line is a linear fit to the relation (including scatter), the dotted black lines indicate the intrinsic scatter, the gray band indicates the quadrature sum of the scatter and the uncertainty on the linear fit, the red dotted line is the linear fit from Hyde & Bernardi (2009a), and the red dashed line is their quadratic fit. We find that the SLACS $\sigma_{e/2}$–M_* relation is consistent with the SDSS relations, although our formal fit is shallower due to our explicit treatment of intrinsic scatter.

(A color version of this figure is available in the online journal.)

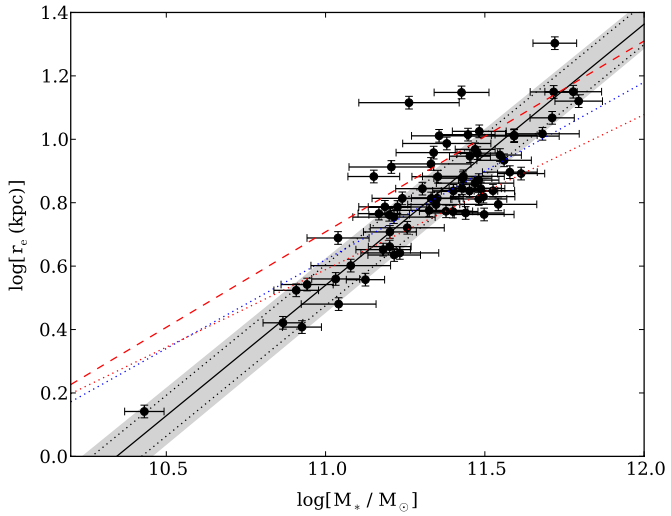

Figure 2. r_e–M_* relation for SLACS lenses. The solid black line is a linear fit to the relation, the dotted black lines indicate the intrinsic scatter, and the gray band indicates the quadrature sum of the scatter and the uncertainty on the linear fit. The blue dotted line is the relation fit by Shen et al. (2003) while the red dotted line is the linear fit from Hyde & Bernardi (2009a) and the red dashed line is their quadratic fit.

(A color version of this figure is available in the online journal.)

object using three independent codes but the codes do not find a significant difference between these six objects and the others. Nevertheless, we use an abundance of caution and exclude these six objects from the fits that include intrinsic scatter, as these objects tend to dominate those relations.

We begin with "traditional" correlations between non-lensing observables in Section 3.1. The main purpose of this section is to compare our inferred correlations with those inferred from samples of non-lens galaxies to test the hypothesis that SLACS lens galaxies are representative of the overall population of massive ETG. Previous SLACS papers have investigated this issue based on a number of tests and have found no evidence for any difference between the SLACS lenses and ETGs with similar velocity dispersions (Treu et al. 2006, 2009; Bolton et al. 2008a; Auger et al. 2009). This study updates and extends some of those tests by considering the larger sample and including in the analysis relations based on stellar mass.

We introduce lensing observables in Section 3.2 to investigate correlations between stellar, total, and dimensional masses, as a means to constrain the virial coefficient, the IMF, and DM content of ETGs. In Section 3.3, we study the distribution of slopes of the total mass-density profile γ', extending the analysis previously published by Koopmans et al. (2009). The goal of this analysis is twofold. From a galaxy formation point of view, the distribution of total mass-density profiles constrains the relative distribution of baryons and DM and therefore constrains quantities such as the star formation efficiency. From the point of view of gravitational lensing studies, the distribution of γ' is an essential piece of information for inferences regarding, e.g., cosmological parameters from gravitational time delays and lens statistics (e.g., Suyu et al. 2010; Dobke & King 2006; Oguri 2007).

Finally, in Section 3.4 we examine variations in central mass-to-light ratio and DM fraction with galaxy global properties again as a means to investigate the IMF and DM content of ETGs.

Table 2
r_e–M_* and $\sigma_{e/2}$–M_* Relations

Y	X	Slope a	Intercept b	Scatter
$\sigma_{e/2}$	M_*	0.24 ± 0.02	2.32 ± 0.01	···
$\sigma_{e/2}$	M_*	0.18 ± 0.03	2.34 ± 0.01	0.04 ± 0.01
r_e	M_*	0.89 ± 0.04	0.52 ± 0.02	···
r_e	M_*	0.81 ± 0.05	0.53 ± 0.02	0.05 ± 0.02

Notes. Fits are of the form $\log Y = a \log X + b$ with M_* in units of $10^{11}\ M_\odot$, $\sigma_{e/2}$ in units of km s^{-1}, and r_e in units of kpc. Each fit is performed twice, either including intrinsic scatter or assuming zero intrinsic scatter. Note that the inclusion of intrinsic scatter has a significant effect on both the size–mass and velocity dispersion–mass relations. These fits are for a Chabrier IMF, but the slope is unaltered assuming a Salpeter IMF.

3.1. Traditional (Non-lensing) Correlations

The $\sigma_{e/2}$–M_* relation is shown in Figure 1 for a Chabrier IMF. The relation is slightly shallower than for SDSS galaxies in general ($a = 0.18 \pm 0.03$, $b = 2.34 \pm 0.01$ with $\sigma_{e/2}$ in units of km s^{-1} and M_* in units of $10^{11}\ M_\odot$), largely due to explicitly including intrinsic scatter in the relation (Table 2). Nevertheless, the Hyde & Bernardi (2009a) relations are acceptable fits to the SLACS data; this is another indication that SLACS lenses constitute a velocity-dispersion-selected subsample of the general population of massive ETGs (Bolton et al. 2008a).

We examine the r_e–M_* relation in Figure 2. We find that the SLACS lenses have a somewhat steeper relation ($a = 0.81 \pm 0.05$, $b = 0.53 \pm 0.02$ for a Chabrier IMF with r_e, measured in kpc and M_* in units of $10^{11}\ M_\odot$; see Table 2) than non-lensing galaxies in SDSS (Shen et al. 2003; Hyde & Bernardi 2009a). This is due in part to the curvature in the r_e–M_* relation; SLACS is dominated by galaxies with $M_* > 10^{11}\ M_\odot$ whereas $10^{11}\ M_\odot$ is the mid-point of the data fit in the SDSS samples. Indeed, we see in Figure 2 that the SLACS lenses follow the high-mass end of the quadratic fit of Hyde & Bernardi (2009a) reasonably well. Additionally, SLACS is effectively a sample selected on velocity dispersion and the typical velocity

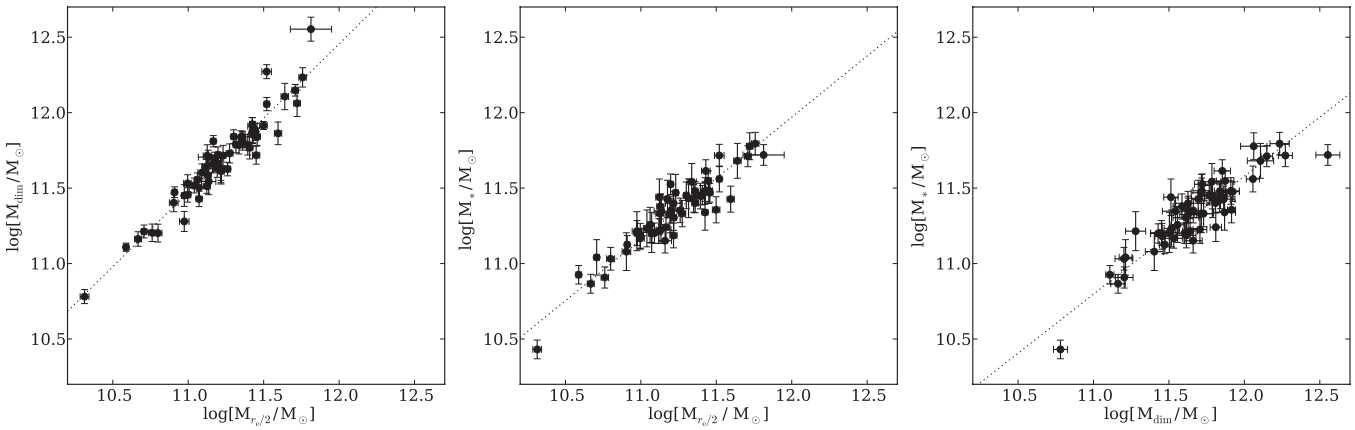

Figure 3. Bivariate correlations between dimensional ($M_{\rm dim}$), total ($M_{r_e/2}$), and stellar mass (M_*). The best-fitting linear relations are shown as dotted lines. Their coefficients are given in Table 3. Note the linear relation between dimensional and total mass, and the nonlinearity of the other two relations. These are consistent with a constant virial coefficient and an increase with mass of the dark matter content and/or stellar initial mass function normalization.

dispersion at fixed effective radius is likely larger than non-lensing SDSS galaxies; this would lead to higher inferred stellar masses at fixed effective radius (see Figure 1), as is seen in our data. Furthermore, Tortora et al. (2009) find a slope of 0.73 ± 0.12 for the r_e–M_* relation of massive ($M_* > 10^{11.1}\ M_\odot$) local ETGs, completely consistent with our results.

There are two components of the velocity dispersion selection function in the SLACS sample. The first comes from the lensing cross section which scales approximately with σ^4. The second one comes from the selection function of the SDSS survey. First, SDSS is a flux-limited sample so that high-luminosity, and therefore high σ, galaxies are overrepresented because they are visible over a larger volume (Hyde & Bernardi 2009a). Second, SDSS has finite resolution and thus ultra-compact galaxies are difficult to identify (e.g., Trujillo et al. 2009; Taylor et al. 2010; Stockton et al. 2010).

We can correct for the lensing bias to make the SLACS sample directly comparable to the parent SDSS sample by weighting each galaxy's contribution to the posterior distribution function by an exponent proportional to σ^{-4} (in χ^2 terms this would be equivalent to weighting each galaxy's contribution to the χ^2 by the same factor). Additionally, we can weight each galaxy by the volume in which it could be observed to provide a more direct comparison with Hyde & Bernardi (2009a). We find that these weighting schemes alter the fits that do not include intrinsic scatter significantly more than the fits with intrinsic scatter; the fits with intrinsic scatter yield consistent results with and without weighting, and we therefore quote the unweighted fits throughout.

3.2. Correlations between Stellar, Dynamical, and Total Mass

Bivariate correlations between mass estimators are shown in Figure 3 and the parameters of linear fits to these relations are given in Table 3. The linear correlation between dimensional mass $M_{\rm dim}$ and lensing (or total) mass $M_{r_e/2}$ indicates that the virial coefficient is constant over the range in mass probed by the SLACS sample, in agreement with our previous result (Bolton et al. 2008b). The average value of the dimensionless parameter akin to the virial coefficient, $\log c_{e2}$, defined by

$$\log M_{r_e/2} = \log \frac{c_{e2} r_e \sigma^2_{e/2}}{2G},$$

is found to be 0.53 ± 0.09 and the scatter is 0.06 ± 0.01 dex; both of these are consistent with our previous measurement (Bolton et al. 2008b). The uniformity of the virial coefficient (i.e., the very small intrinsic scatter) does not imply exact scale invariance of the mass-dynamical structure of ETGs. In fact, as shown by Nipoti et al. (2008), the observed virial coefficient can be reproduced by a variety of two component mass models with a broad distribution of central DM fractions. The uniformity of the virial coefficient, however, restricts the possible range of acceptable models for ETGs; in particular, models with extreme orbital anisotropies or that depart significantly from an isothermal total mass-density profile are ruled out (Nipoti et al. 2008).

Table 3
Correlations between Masses

Y	X	Slope	Intercept	Scatter
$M_{\rm dim}$	$M_{r_e/2}$	0.97 ± 0.02	0.51 ± 0.03	···
$M_{\rm dim}$	$M_{r_e/2}$	0.98 ± 0.03	0.50 ± 0.04	0.06 ± 0.01
M_*	$M_{r_e/2}$	0.81 ± 0.03	0.35 ± 0.04	···
M_*	$M_{r_e/2}$	0.80 ± 0.04	0.36 ± 0.05	0.03 ± 0.02
M_*	$M_{\rm dim}$	0.80 ± 0.04	-0.01 ± 0.06	···
M_*	$M_{\rm dim}$	0.79 ± 0.04	0.01 ± 0.08	0.04 ± 0.02

Notes. All fits are done in logarithmic scales and using masses in units of 10^{10} $M_\odot$, to reduce covariance. Fits without and with intrinsic scatter are given for each pairwise combination. For example, the first line contains the results of fitting $\log M_{\rm dim}/10^{10}\ M_\odot = a \log M_{r_e/2}/10^{10}\ M_\odot + b$, where a and b are the slope and intercept, respectively. The second line adds an additional Gaussian component with average zero to represent intrinsic scatter. The width of the Gaussian intrinsic scatter is 0.06 ± 0.01 dex.

The correlation between total mass and stellar mass has the same amount of intrinsic scatter as the one with dimensional mass, once the larger errors associated with stellar mass are accounted for. However, the slope of the correlation differs significantly from unity. This is consistent with the well-known "tilted" slope of the correlation between dynamical and stellar mass (Faber et al. 1987; Cappellari et al. 2006; Gallazzi et al. 2006; Bundy et al. 2007; Rettura et al. 2006; Graves & Faber 2010) and can be explained in terms of a varying DM fraction and/or stellar IMF normalization with mass, in the sense that more massive galaxies have a higher fraction of (baryonic or otherwise) DM. Interestingly, however, the small intrinsic scatter indicates that *at fixed mass* the DM fraction and/or stellar IMF normalization are tightly constrained. We will return to these points in Section 3.4.

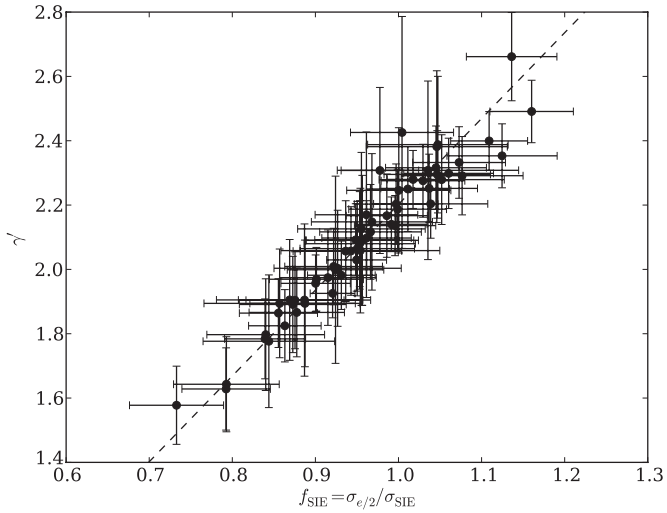

Figure 4. Relationship between the ratio of the observed stellar velocity dispersion and the SIE model velocity dispersion, $f_{\rm SIE} \equiv \sigma_{e/2}/\sigma_{\rm SIE}$, and the logarithmic density slope γ'. The correlation is very tight, with evidence for little intrinsic scatter ($\sigma_{\rm int} = 0.02$). Note that although the errors on f and γ' are strongly correlated, our analysis takes this correlation into account and finds a significant excess correlation. The tightness of the relation implies that $f_{\rm SIE}$ can be a useful proxy for γ' without performing the joint lensing and dynamics modeling.

3.3. Correlations with the Slope of the Total Mass-density Profile

We first examine the overall distribution of slopes of the mass-density profile in a joint framework wherein the γ' of all of the early-type lenses are assumed to be drawn from a normal distribution parameterized by an average γ'_0 and a dispersion σ'_γ. We find $\gamma'_0 = 2.078 \pm 0.027$ and $\sigma'_\gamma = 0.16 \pm 0.02$, consistent with and extending the results of Koopmans et al. (2009). The SLACS early-type lenses appear to be slightly super-isothermal (i.e., the density profiles are typically steeper than isothermal by $\sim$5%) with an intrinsic spread of $\approx$ 10%. We note, however, that we have assumed that the galaxies are isotropic; as discussed in Koopmans et al. (2009), a modest amount of radial anisotropy ($\beta \lesssim 0.5$; consistent with Gerhard et al. 2001) is sufficient to produce an isothermal slope, $\gamma'_0 = 2$. We cannot directly probe the anisotropy with our data (but see Koopmans et al. 2009, which provides an indirect constraint) and we therefore impose the isotropic model.

It was previously found that the ratio of the observed stellar velocity dispersion and the SIE model velocity dispersion, $f_{\rm SIE} \equiv \sigma_{e/2}/\sigma_{\rm SIE}$, is strongly correlated with the logarithmic density slope (Treu et al. 2009). Our updated analysis confirms this result (Figure 4) and the best-fit linear relation, taking into account the covariance between $f_{\rm SIE}$ and γ', is given by $\gamma' - 2 = (2.67 \pm 0.15)(f_{\rm SIE} - 1) + (0.20 \pm 0.01)$. Note that this trend is a natural consequence of how γ' is determined and does not provide any significant physical insights; instead, it provides a useful shortcut for determining the power-law slope from $\sigma_{e/2}$ and $\sigma_{\rm SIE}$ without needing to perform Jeans modeling.

Koopmans et al. (2009) found that the power-law slope did not correlate strongly with many of the global galaxy observables, including redshift, the ratio of the Einstein and effective radii, the central lensing mass, and $\sigma_{\rm SIE}$. This updated analysis does not substantially change these results since we are only introducing 20% more systems. However, we now also investigate correlations with r_e, $\sigma_{e/2}$, and the central surface mass density $\Sigma_{\rm tot} \equiv M_{r_e/2}/r_e^2$. We find non-negligible correlations (non-zero slopes with greater than 3σ significance) with r_e and $\Sigma_{\rm tot}$ but no clear trend with $\sigma_{e/2}$ (Figure 5); the correlation with $\Sigma_{\rm tot}$ is the tightest and most significant (Table 4). This is expected, since a steeper mass-density profile implies a higher central surface mass density, and explains at least in part the intrinsic dispersion in the average mass-density profile. However, the residual intrinsic dispersion (0.12, i.e., 6% in slope) indicates that there may be additional observables that correlate with the inferred slope. One such parameter could be local environment, due to tidal effects on the outer halos or to contamination to the lensing convergence by external mass along the line of sight. The former has been tentatively detected using the SLACS sample at marginal levels of significance (Auger 2008; Treu et al. 2009), and it has been observed in clusters (e.g., Natarajan et al. 2009). The latter does not seem to be significant in the SLACS sample, as inferred from the minimal level of misalignment between the major axis of the light and mass. Another element that may contribute to the scatter is anisotropy of the stellar orbits. However, higher precision measurements will be required to determine whether the residual scatter is stochastic in nature and/or if there are residual and undetected small systematic trends.

There is tentative evidence for a slight anti-correlation between γ' and the total and stellar masses, as one might infer from the trends with radius and surface mass density, although neither of these anti-correlations between slope and mass are statistically significant given our sample size and data quality. Nevertheless we note that an anti-correlation between mass and density slope can arise as a result of mergers (e.g.,

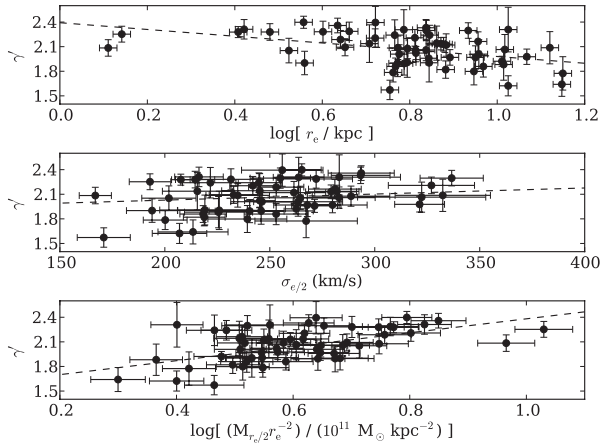

Figure 5. Correlations between r_e, $\sigma_{e/2}$, and $\Sigma_{\rm tot}$ (see Table 4 for the linear fits). The correlation with $\sigma_{e/2}$ is not significant although the r_e and $\Sigma_{\rm tot}$ correlations are found at greater than 3σ significance. All correlations show significant scatter, and the effective radius correlation is somewhat weaker than the central surface mass-density correlation. This latter correlation is expected; steeper power-law slopes imply higher central concentrations, and higher central concentrations imply increased central surface mass densities.

Table 4
Correlations with $\gamma' - 2$

X	Slope	Intercept	Scatter
$\log r_e$	-0.41 ± 0.12	0.39 ± 0.10	0.14 ± 0.02
$\sigma_{e/2}$	0.07 ± 0.08	-0.12 ± 0.21	0.17 ± 0.02
$\Sigma_{\rm tot}$	0.85 ± 0.19	-0.47 ± 0.12	0.12 ± 0.02

Note. r_e is in units of kpc, $\sigma_{e/2}$ is in units of 100 km s^{-1}, and $\Sigma_{\rm tot}$ is in units of $10^{11}\ M_\odot$ kpc^{-2}.

Table 5
log $[M/L]$ Linear Relations for SLACS Lenses

X	Stellar M/L			Total M/L		
	a	b	$\sigma_{\rm int}$	a	b	$\sigma_{\rm int}$
L_B (B band)	0.02 ± 0.04	0.59 ± 0.03	0.02 ± 0.01	0.19 ± 0.06	0.85 ± 0.05	0.09 ± 0.01
L_B (V band)	0.01 ± 0.04	0.49 ± 0.03	0.01 ± 0.01	0.19 ± 0.06	0.75 ± 0.05	0.09 ± 0.01
L_V (B band)	0.03 ± 0.04	0.58 ± 0.04	0.02 ± 0.01	0.21 ± 0.06	0.82 ± 0.05	0.09 ± 0.01
L_V (V band)	0.02 ± 0.03	0.49 ± 0.03	0.01 ± 0.01	0.20 ± 0.06	0.71 ± 0.05	0.09 ± 0.01
$\sigma_{e/2}$ (B band)	0.26 ± 0.16	0.50 ± 0.07	0.02 ± 0.01	0.89 ± 0.23	0.63 ± 0.09	0.09 ± 0.01
$\sigma_{e/2}$ (V band)	0.19 ± 0.14	0.42 ± 0.06	0.01 ± 0.01	0.81 ± 0.23	0.56 ± 0.09	0.09 ± 0.01
$M_{\rm dim}$ (B band)	0.03 ± 0.03	0.59 ± 0.02	0.02 ± 0.01	0.24 ± 0.05	0.83 ± 0.03	0.08 ± 0.01
$M_{\rm dim}$ (V band)	0.02 ± 0.03	0.49 ± 0.02	0.01 ± 0.01	0.23 ± 0.04	0.72 ± 0.03	0.08 ± 0.01
M_* (B band)	0.07 ± 0.04	0.58 ± 0.02	0.02 ± 0.01	0.22 ± 0.06	0.91 ± 0.02	0.09 ± 0.01
M_* (V band)	0.05 ± 0.03	0.48 ± 0.01	0.01 ± 0.01	0.21 ± 0.06	0.81 ± 0.02	0.09 ± 0.01
$M_{r_e/2}$ (B band)	0.04 ± 0.03	0.60 ± 0.01	0.02 ± 0.01	0.27 ± 0.04	0.93 ± 0.01	0.07 ± 0.01
$M_{r_e/2}$ (V band)	0.03 ± 0.03	0.50 ± 0.01	0.01 ± 0.01	0.26 ± 0.04	0.83 ± 0.01	0.07 ± 0.01

Notes. Fits are of the form $\log [M/L/(M/L)_\odot] = a^*\log [X] + b$ and the stellar M/L is determined assuming a Chabrier IMF. L_B and L_V are in units of $10^{10}\ L_\odot$, $\sigma_{e/2}$ is in units of 100 km s^{-1}, and the masses (M_*, $M_{\rm dim}$, and $M_{r_e/2}$) are in units of $10^{11}\ M_\odot$.

Table 6
$f_{\rm DM}$ Linear Relations for SLACS Lenses

X	Chabrier IMF			Salpeter IMF		
	a	b	$\sigma_{\rm int}$	a	b	$\sigma_{\rm int}$
L_B	0.16 ± 0.06	0.47 ± 0.05	0.05 ± 0.02	0.28 ± 0.10	0.08 ± 0.08	0.09 ± 0.03
L_V	0.16 ± 0.06	0.46 ± 0.05	0.05 ± 0.02	0.28 ± 0.10	0.04 ± 0.09	0.09 ± 0.03
$\sigma_{e/2}$	0.46 ± 0.22	0.40 ± 0.09	0.06 ± 0.02	0.80 ± 0.44	-0.05 ± 0.18	0.11 ± 0.03
r_e	0.28 ± 0.05	0.36 ± 0.05	0.03 ± 0.02	0.49 ± 0.10	-0.13 ± 0.09	0.06 ± 0.03
M_*	0.13 ± 0.06	0.54 ± 0.03	0.06 ± 0.02	0.23 ± 0.11	0.14 ± 0.07	0.10 ± 0.03
$M_{r_e/2}$	0.20 ± 0.04	0.54 ± 0.02	0.03 ± 0.02	0.36 ± 0.07	0.20 ± 0.03	0.06 ± 0.03

Notes. Fits are of the form $f_{\rm DM} = a^*\log [X] + b$. L_B and L_V are in units of $10^{10}\ L_\odot$, $\sigma_{e/2}$ is in units of 100 km s^{-1}, r_e is in kpc, and M_* and $M_{r_e/2}$ are in units of $10^{11}\ M_\odot$.

Boylan-Kolchin & Ma 2004), although analytic models of halo collapse may predict a *positive* correlation between the mass and central density slope of the DM halo (e.g., Del Popolo & Kroupa 2009).

We have previously combined the SLACS lenses with a higher-redshift set of lenses from the Lensing Structure and Dynamics (LSD; Treu & Koopmans 2004) sample and found marginal evidence that the central mass-density slope evolves with redshift (Koopmans et al. 2006). However, the relationship between γ' and $\Sigma_{\rm tot}$ was not explicitly accounted for in that analysis; a full investigation of the evolution of γ' including this effect will require an expanded sample of high-redshift lenses.

3.4. Central Mass-to-Light Ratios and Dark Matter Fraction Correlations

The SLACS data set presents a unique opportunity to investigate the central mass-to-light ratio and DM fraction in galaxies beyond the local universe. We first look at the relationship between M/L and six other parameters: B-band luminosity at $z = 0$, V-band luminosity at $z = 0$, $\sigma_{e/2}$, $M_{\rm dim}$, M_*, and $M_{r_e/2}$. These trends are shown in Figure 6 and listed in Table 5. It is clear that there is a significant trend between all of these parameters and total M/L, while M_*/L is, at the 2σ level, independent of the quantities investigated, and we also note that M_*/L and the total M/L correlate more strongly with $\sigma_{e/2}$ than with mass or luminosity. These results are in excellent agreement with Cappellari et al. (2006) and Tortora et al. (2009), who investigate the stellar M/L and dynamical M/L for samples of E and S0 galaxies, and with results from the FP and M$_*$P of SDSS galaxies (Hyde & Bernardi 2009b; Graves & Faber 2010). However, Grillo & Gobat (2010) find a somewhat steeper trend between M_* and M_*/L_B for the SLACS lenses ($a = 0.18$), which we attribute to differences in the stellar mass determination due to assumptions about age and metallicity (e.g., Auger et al. 2009). For very massive ETGs like the ones in the SLACS sample, the differences in stellar population properties are not sufficiently large to account for large changes in the stellar M/L with a fixed IMF. Conversely, the total mass-to-light ratio clearly increases with total stellar mass, possibly as a result of increased DM or varying stellar IMF. The stellar M/L relations are all consistent with no intrinsic scatter, indicating a remarkable homogeneity in the stellar populations of these galaxies. The total M/L trends, on the other hand, exhibit 0.07–0.09 dex of intrinsic scatter; this is expected since the various parameter planes (Section 4) demonstrate that three parameters are required to adequately describe ETGs (e.g., Graves & Faber 2010).

In Figure 7, we show the trends in the projected DM fraction with the total mass inferred from lensing, the stellar mass, the observed stellar velocity dispersion from SDSS, the effective radius, and the B- and V-band luminosities evolved to $z = 0$. Linear fits to these relations are provided in Table 6, and we see a clear trend of increasing DM fraction with each of these quantities. Curiously, Grillo (2010) finds a negative slope in the relation between the DM fraction within r_e (note the different

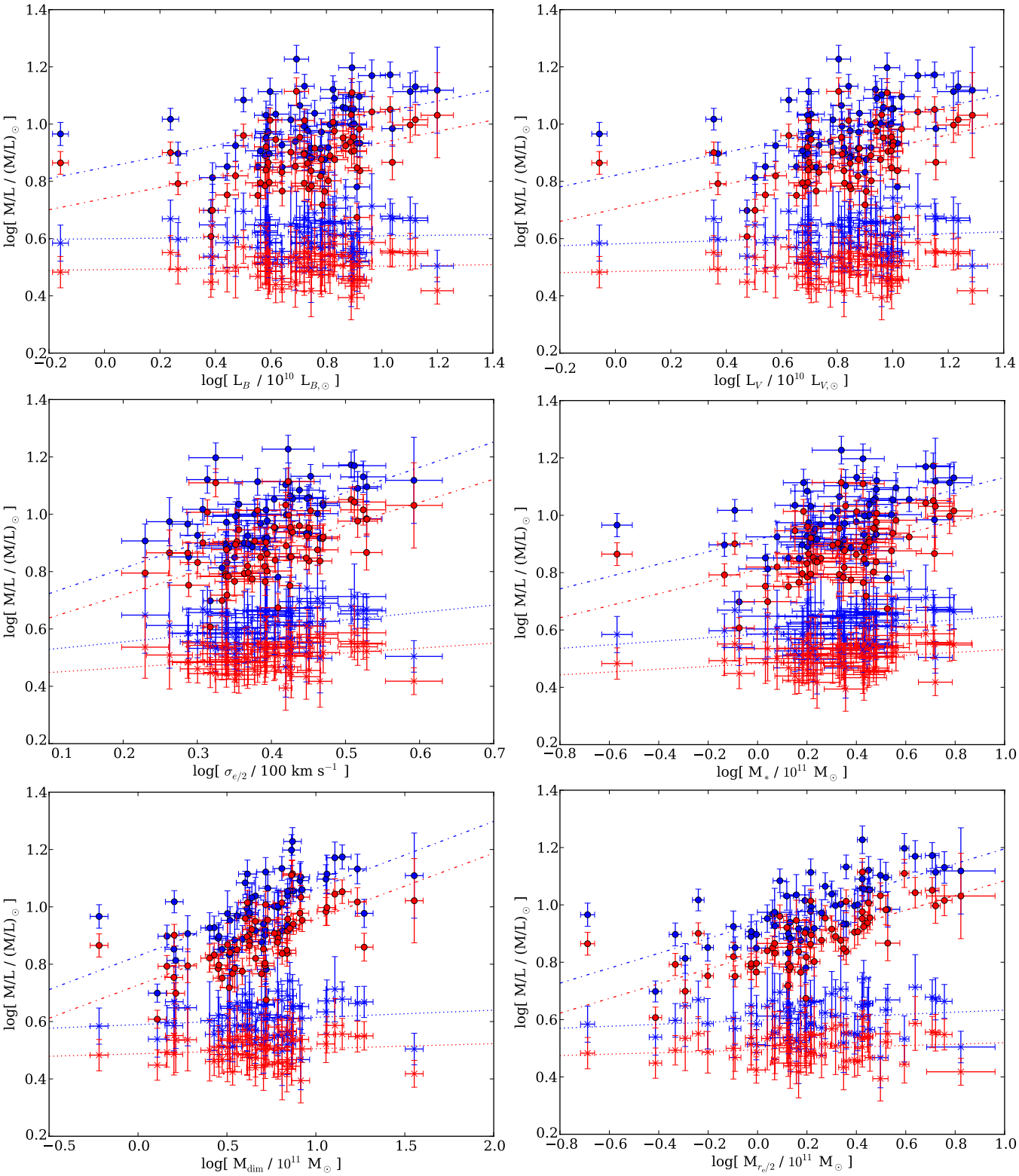

Figure 6. Relations between the stellar (crosses) and total (points) M/L in the B (blue) and V (red) bands for the SLACS lenses. A Chabrier IMF has been assumed for the stellar M/L. The dotted lines are linear fits to the stellar M/L relations and dash-dotted lines are linear fits to the total M/L relations.

(A color version of this figure is available in the online journal.)

aperture used) and stellar mass, although other authors who use the r_e aperture find results consistent with ours (e.g., Cardone et al. 2009; Cardone & Tortora 2010).

The most significant trends are with effective radius and total mass (also see Napolitano et al. 2010; Tortora et al. 2010), indicating that these parameters govern the central DM fraction. These parameters are also consistent with having no intrinsic scatter at the 95% confidence level (i.e., $\sigma_{\rm int}$ is within 2σ of 0), although the errors are large. We note that part of this scatter may also be due to the inadequacy of a linear fit; this

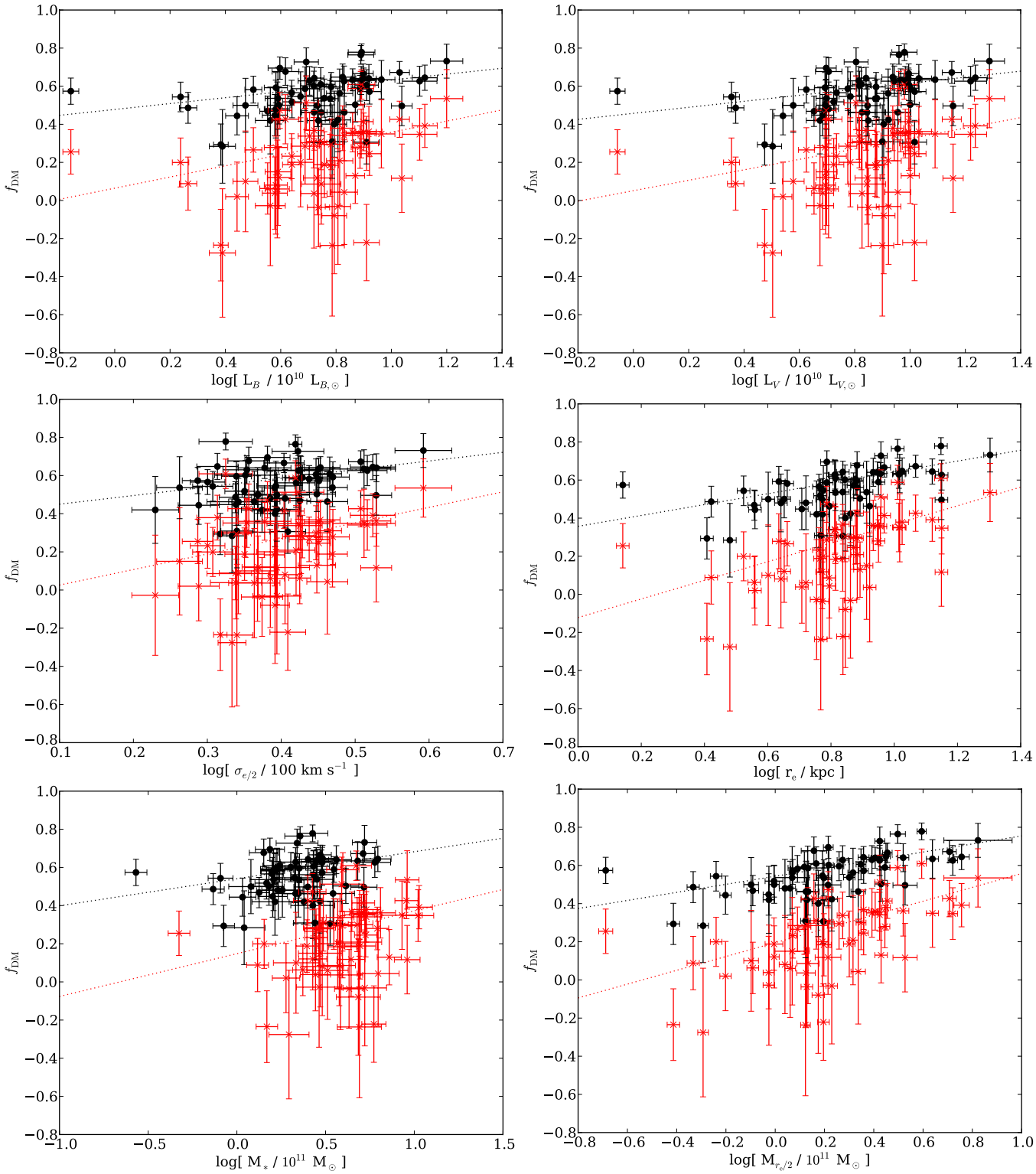

Figure 7. Relations between the projected dark matter fraction within half of the effective radius and L_B, L_V, $\sigma_{e/2}$, r_e, M_*, and $M_{re/2}$. Red points are for a Salpeter IMF and black points are for a Chabrier IMF; the most significant trends are with r_e and $M_{re/2}$.

(A color version of this figure is available in the online journal.)

is most clear for the Salpeter relations, which would indicate a physically impossible negative DM fraction if the linear trend is extrapolated below a stellar mass of $\sim 10^{10.5}\,M_\odot$. A more appropriate model that relates the baryonic mass to the total mass (and thereby requires the baryons to be less than the total mass) is explored in Auger et al. (2010).

4. CORRELATIONS IN THREE OR MORE DIMENSIONS

The SLACS lens galaxies have previously been shown to lie on the FP (Treu et al. 2006; Bolton et al. 2008b) and on the MP (Bolton et al. 2007, 2008b). We now revisit these relations with the enlarged SLACS sample and self-consistently

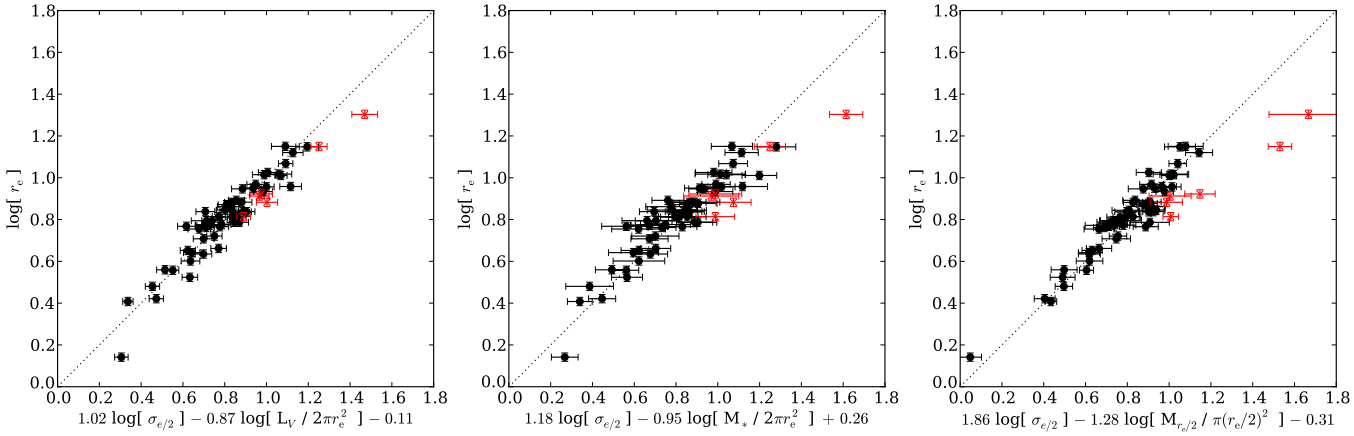

Figure 8. FP, M_*P, and MP relations for the SLACS lenses. All three planes show little intrinsic scatter ($\sigma_{\rm int} \lesssim 0.05$) and the FP and M_*P are aligned well. The MP is found to be offset from the FP and M_*P but is approximately aligned with the virial plane. The red points indicate the six galaxies which are outliers on the fundamental hyper-plane and are not included in the fits.

(A color version of this figure is available in the online journal.)

evolved luminosities, superceding our previous analysis. We also investigate other scaling relations involving stellar mass, such as the stellar mass including the stellar mass plane (M_*P) and a new correlation in a higher-dimensional parameter space, which we call the FPH.

4.1. Fundamental and Mass Planes

We fit the parameter plane relations with the form

$$\log r_e = \alpha^{\rm pp} \log \sigma_{e/2} + \beta^{\rm pp} \log \Lambda + \gamma^{\rm pp}, \qquad (2)$$

where Λ represents the average surface brightness within r_e, the average stellar mass surface density within r_e, or the average total mass surface density within $r_e/2$. The units used for the fits are kpc for r_e, 100 km s^{-1} for $\sigma_{e/2}$, $10^9\ L_\odot$ for the luminosity, $10^9\ M_\odot$ for the stellar mass, and $10^{10}\ M_\odot$ for the total mass. The intrinsic scatter is given in units of $\log r_e$. The inferred parameter planes are shown in Figure 8 and illustrate the small intrinsic scatter found in these relations.

We find that the FP relation is somewhat tilted with respect to previous analyses (e.g., Bolton et al. 2008b) if we allow the intrinsic scatter to be a free parameter of our fit (see Table 7). If we do not fit for intrinsic scatter (that is, if we impose that the intrinsic scatter is zero), we recover an FP consistent with other determinations (Bolton et al. 2008b; Hyde & Bernardi 2009b). This illustrates the importance of explicitly accounting for intrinsic scatter in the fit, even when it is small like in the case of the FP. As a further consistency check, we repeated the fit of the FP parameters applying the σ^{-4} scaling to account for the velocity dispersion selection of the SLACS sample, and we find that the changes are insignificant. This is consistent with the findings of Hyde & Bernardi (2009b), since our fitting method is closer to their "direct" fit than to their orthogonal fit. The non-zero scatter of the FP confirms previous results and is consistent with being due to a combination of stellar population differences and structural differences. The availability of stellar mass and total mass diagnostics allows us to break this degeneracy as we discuss in the rest of this section.

The coefficients for the M_*P plane are independent of the choice of IMF for the SPS models (the normalization term changes by ≈ 0.25, as is expected for Chabrier and Salpeter IMFs when $\beta \approx -1$). It has previously been found that the M_*P (where M_* is inferred from SPS models) lies closer to the virial plane ($\alpha = 2$; $\beta = -1$) than the FP (Hyde & Bernardi 2009b), although we find in our data that the FP and M_*P are approximately aligned. We note, however, that the M_*P is consistent with having no intrinsic scatter ($\sigma_{\rm int} = 0.020 \pm 0.014$) while the FP has intrinsic scatter of $\sigma_{\rm int} = 0.049 \pm 0.009$ dex; this implies that the scatter in the FP is largely driven by small differences in stellar populations (e.g., age or metallicity) for massive galaxies, rather than from structural properties (i.e., differences in DM content or the virial coefficient at a fixed size and velocity dispersion).

Table 7
Parameter Planes for SLACS Lenses

Plane	$\alpha^{\rm pp}$	$\beta^{\rm pp}$	$\gamma^{\rm pp}$	$\sigma_{\rm int}$
FP	1.189 ± 0.141	-0.885 ± 0.041	-0.185 ± 0.047	···
M_*P	1.191 ± 0.221	-0.971 ± 0.073	0.257 ± 0.088	···
MP	1.829 ± 0.133	-1.301 ± 0.061	-0.301 ± 0.055	···
FP	1.020 ± 0.203	-0.872 ± 0.052	-0.108 ± 0.076	0.049 ± 0.009
M_*P	1.185 ± 0.214	-0.952 ± 0.074	0.261 ± 0.085	0.020 ± 0.014
MP	1.857 ± 0.136	-1.279 ± 0.065	-0.312 ± 0.056	0.013 ± 0.010

Notes. Fits are of the form given in Equation (2), with r_e in units of kpc, $\sigma_{e/2}$ in units of 100 km s^{-1}, V-band luminosity and stellar mass in units of $10^9\ L_\odot$ and $10^9\ M_\odot$, respectively, and total mass in units of $10^{10}\ M_\odot$. The first three fits are without intrinsic scatter while the latter three explicitly include scatter using the model of Kelly (2007).

The MP is also consistent with having no scatter (Table 7) but is substantially misaligned with the FP and M_*P; instead, the MP is approximately aligned with the virial plane (as was found in Bolton et al. 2007, 2008b; also see Koopmans et al. 2009, where this plane included γ'). The offset with respect to the FP and M_*P is consistent with the bivariate relations (e.g., the middle panel of Figure 3 and the total M/L trends of Figure 6), while the slight offset from the virial plane may be related to the systematic deviation of the central mass-density profile from isothermality (e.g., Figure 5) or anisotropy. The MP is also found to be consistent with no intrinsic scatter, although the errors are large.

4.2. The Fundamental Hyper-plane

The M_*P and MP are found to have little intrinsic scatter but very different orientations in size–velocity dispersion–mass space. We would like to know whether the remaining scatter in

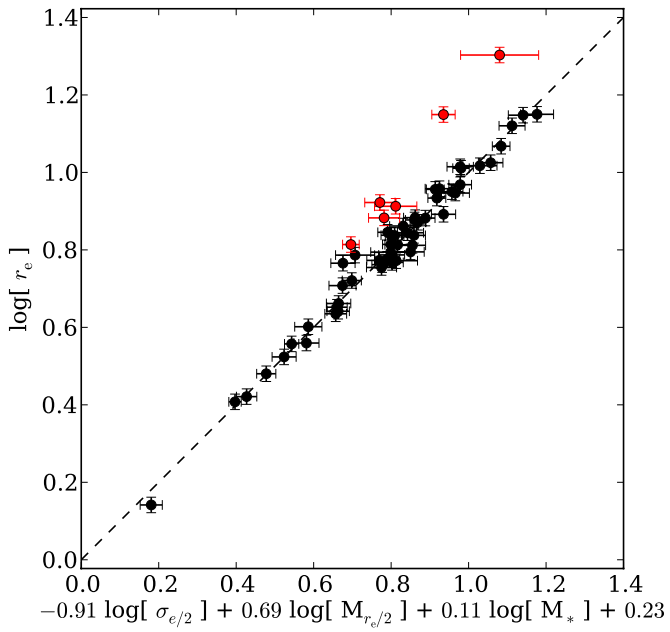

Figure 9. Relationship between the size, velocity dispersion, and mass (both stellar and total) of SLACS lenses. The red points are outliers that are rejected from the fit, which is found to be consistent with less than 3.5% intrinsic scatter at 95% confidence.

(A color version of this figure is available in the online journal.)

these planes is due to a non-trivial relationship between $M_{r_e/2}$ and M_*. We therefore explicitly explore the relative importance of the stellar and total mass on the structure of ETGs. In particular, we consider the relationship between the effective radius, velocity dispersion, central stellar mass, and central total mass by assuming a relation of the form

$$\log r_e = \alpha^{\rm hp} \log \sigma_{e/2} + \beta^{\rm hp} \log M_{r_e/2} + \gamma^{\rm hp} \log M_* + \delta^{\rm hp}, \quad (3)$$

where M_* is now the stellar mass within half the effective radius to ensure consistency with the lensing determined total mass. An initial fit to this relation finds that a small number of galaxies, six in total, are significant outliers (greater than $3\sigma_{\rm int}$, where $\sigma_{\rm int} = 0.03$ for the initial fit). We re-fit the relation without these objects and find a substantially tighter relation with approximately the same coefficients but substantially decreased scatter. We therefore suspect that these objects have aberrant velocity dispersions and have therefore excluded them from our analysis, as discussed in Section 2.

The best-fit relation for the FPH, with r_e measured in kpc, $\sigma_{e/2}$ in 100 km s^{-1}, and both stellar and total mass in $10^{10}\,M_\odot$, is given by

$$\log r_e = (-0.91 \pm 0.10) \log \sigma_{e/2} + (0.69 \pm 0.04) \log M_{r_e/2} + (0.11 \pm 0.06) \log M_* + (0.23 \pm 0.03) \quad (4)$$

with intrinsic scatter $\sigma_{\rm int} = 0.007 \pm 0.005$, and the fit is shown in Figure 9. The dominant terms are the central velocity dispersion and central total mass, while the stellar mass only has a marginal role and is consistent with being unimportant at the 2σ level (that is, the coefficient for the M_* term is within 2σ of zero).

5. DISCUSSION

Before discussing our results in the broader context of studies of the structure formation and evolution of ETGs, it is essential to test whether the SLACS ETGs are indeed representative of the overall population. In previous papers, we have shown that SLACS lens galaxies cannot be distinguished from control samples of ETGs selected from the SDSS archive to have the same stellar velocity dispersion and redshift (Treu et al. 2006; Bolton et al. 2008a; Auger et al. 2009). In this paper, we further refine these tests by considering the complete SLACS sample of 73 ETGs, and testing a number of correlations, including the FP, the M$_*$P, and their projections, the M_*–r_e and M_*–σ correlations. Once again we do not find any substantial difference between the correlations inferred for our sample and for SDSS-selected samples of non-lenses. Having found no significant evidence of a systematic difference, we can safely assert that SLACS lenses are representative of the entire population of massive ETGs and proceed to interpret our results.

5.1. The "Bulge-halo" Conspiracy, and Implications of (Small) Departures from it

The first key result of this study, building on previous SLACS papers, is the precise measurement of the so-called bulge-halo conspiracy and its tightness. In short, although mass clearly does not follow light and an extended DM halo is needed to reproduce simultaneously the lensing and dynamical constraints, the two components add up to form almost exactly an isothermal total mass-density profile in the inner regions of galaxies ($\rho_{\rm tot} \propto r^{-\gamma'}$, with $\gamma' = 2$). This is remarkable, since neither component is a single power law, and there is no simple fundamental reason why this should be the case, although general dynamical arguments based on incomplete violent relaxation suggest that the isothermal sphere is a form of dynamical attractor (e.g., Gunn 1977; Dekel et al. 1981; van Albada 1982; Bertschinger 1985; Loeb & Peebles 2003). In addition, models based on simple prescriptions for baryonic condensation (e.g., Gnedin et al. 2004) seem to suggest that it is possible to obtain close-to-isothermal total mass-density profiles starting from cosmologically motivated DM halos (Jiang & Kochanek 2007; Humphrey & Buote 2010).

The resulting isothermal profile cannot be explained based purely on dissipationless processes. In fact, dissipationless processes in a cosmological setting would tend to produce inner density profiles close to $\gamma' = 1$ or even flatter (Navarro et al. 2004). However, once the isothermal profile is established via dissipational processes (e.g., Ciotti et al. 2007; Robertson et al. 2006), collisionless "dry" mergers preserve it quite accurately, introducing a small amount of scatter, consistent with the observed value (Nipoti et al. 2009b). An interpretation of the bulge-halo conspiracy and its possible origins are discussed at lengths in previous SLACS papers (e.g., Koopmans et al. 2006) and will not be repeated here.

However, the precision achieved in this and previous SLACS studies (e.g., Koopmans et al. 2006, 2009) allows us to highlight the importance of the small but significant observed departures from the bulge-halo conspiracy. First, the average mass-density profile is not exactly isothermal but slightly steeper, $\gamma' = 2.078 \pm 0.027$. Second, there is evidence for non-negligible intrinsic scatter 0.16 ± 0.02. Third, there is tentative evidence for a mild dependency between γ' on galaxy properties, such as radius or central mass density.

The first fact has important implications for gravitational lens studies, particularly those trying to infer cosmography from gravitational time delays. Given the known degeneracy between slope of the mass-density profile and time delays (e.g., Wucknitz 2002), if one assumes an isothermal prior then the inferred

Hubble constant will typically be biased low by 10% if no other direct measure of the mass slope is available (see Oguri 2007; Dobke & King 2006; Kochanek 2006; Treu 2010, and references therein). Additionally, due to the intrinsic scatter, estimates of the Hubble constant from a single lens can be off by 20% if an isothermal model is assumed and not independently constrained. Note, however, that these arguments are based on our assumption of isotropic orbits; anisotropy could change these biases considerably (e.g., Koopmans et al. 2009) and must be constrained in more detail in future work. Nevertheless, additional external information on the mass-density slope, such as that inferred from multiply imaged extended sources (Warren & Dye 2003; Suyu et al. 2006) and from stellar kinematics (Treu & Koopmans 2002; Koopmans et al. 2003), can help to break these degeneracies and provide robust estimates of cosmological parameters (e.g., Suyu et al. 2010).

The average slope $\gamma' = 2.078 \pm 0.027$ is marginally steeper than the slopes found by Koopmans et al. (2006) for a subset of the SLACS lenses and by Humphrey & Buote (2010), who use X-ray temperature and density profiles to find the best-fit power slope for the mass distributions of four ETGs. However, the more flexible mass model employed by Cardone et al. (2009) suggests a somewhat steeper slope of $\sim$2.17 at the Einstein radii of 21 SLACS lenses. Suyu et al. (2010) use very deep *HST* observations along with lensing time delays and stellar kinematics to find that the slope of the lens B1608+656 is in excellent agreement with the average SLACS slope, although B1608+656 is at a higher redshift ($z = 0.63$) than the SLACS lenses and the typical central mass slope may evolve with redshift (e.g., Koopmans et al. 2006).

From the point of view of galaxy formation, the intrinsic scatter and the correlations between γ' and galaxy properties are the most interesting new elements (also see Humphrey & Buote 2010). The tightness imposes a constraint on the number of major merging events, as well as on the diversity of formation histories. We will return to this point later in Section 5.3 in the context of the tightness of the empirical correlation. The dependency of mass-density slope on galaxy parameters is another piece of evidence supporting the idea that ETGs are not a homologous family from a structural point of view. Both facts provide an interesting constraint for numerical simulations that have sufficient resolution and baryonic physics to simulate the inner regions of ETGs (e.g., Robertson et al. 2006; Naab et al. 2007; González-García et al. 2009; Lackner & Ostriker 2010). Small departures from regularity in the end may be the key to understanding the details of ETGs formation (Kormendy et al. 2009).

5.2. Non-triviality of Empirical Correlations

The second key property of ETGs that we quantify in this study is the degree to which their internal structure changes as a function of mass or size. There are many ways to express this, including the observed "tilt" of the FP and the mass-dependent correlation between stellar mass and dynamical mass. The lensing observables from the SLACS sample allow us to add additional information and breaking some of the degeneracies in the interpretation of these trends. We find that, over the range of masses probed, the *total* amount of mass is a nonlinear function of stellar mass, while the virial coefficient is approximately constant. Similarly, we find that the trends cannot be due to changes in stellar mass-to-light ratio for a fixed IMF. In fact, the M_*/L inferred from SPS models is approximately the same for all SLACS ETGs (see also Tortora et al. 2009; Grillo et al. 2009), consistent with the homogeneity of old stellar populations present in massive ETGs (e.g., Thomas et al. 2005). The fact that the *total* M/L varies strongly as a function of mass, velocity dispersion, and luminosity means that more massive galaxies have higher total M/L than less massive systems. This suggests that either the central DM fraction or the IMF is a strong function of mass (e.g., Treu et al. 2010; Tortora et al. 2009). In other words, it is the central fraction of DM, *either baryonic or non-baryonic*, that increases with galactic stellar mass.

These trends have long been connected with the presence of some characteristic scale in the formation process of ETGs that may be due to baryonic physics. For example, the increase in cooling timescales for the hot gas going from the lower mass to the higher mass ETGs significantly changes the efficiency of converting baryons into stars and therefore affects the DM fraction in the central regions (e.g., Robertson et al. 2006, and references therein). Additionally, changes in the modes of star formation that are responsible for variations in chemical abundances could perhaps induce variations in the stellar IMF (but see Graves & Faber 2010 for a discussion). However, collisionless processes can also contribute to the emergence of changes in structural properties with mass. For example, the fraction of DM within the cylinder of radius equal to a fixed fraction of the effective radius changes during dry mergers as a result of the increase in effective radius (Nipoti et al. 2009b).

Interestingly, the observed trends cannot be explained by a single phenomenon (for example, an increase in star formation efficiency with total mass) as we know that ETGs occupy at least a two-dimensional subset of parameter space even when stellar population effects are excluded by purely structural correlations like the MP and (assuming robust SPS models and ignoring the unknown normalization due to the IMF) the stellar mass plane. It appears that velocity dispersion as well as size (or dynamical mass) are needed to fully specify the dynamical properties of an ETG. Furthermore, neither the MP nor the M_*P appear to have intrinsic scatter. Thus, remarkably, it appears that two parameters are not only necessary but also sufficient to fully specify the internal structure of a massive ETG within our observational errors. Finally, when we construct a direct relationship between the structural parameters (effective radius, velocity dispersion, stellar mass, and central total mass) of the SLACS lenses (Equation (4)), we find that the relationship is nearly independent of the stellar mass. In terms of observables for non-lens galaxies, the driving parameters are size and stellar velocity dispersion, not stellar mass.

5.3. Tightness of Empirical Correlations

The third key feature of ETGs addressed in this study is the tightness of the empirical correlations. Traditional non-lensing correlations, such as the FP, have small but non-zero intrinsic scatter (e.g., Jorgensen et al. 1996; Hyde & Bernardi 2009b). Graves & Faber (2010) have recently emphasized the presence of intrinsic scatter in the M_*P relation at the level of 0.02–0.03 dex, discussing several interpretations in terms of diversity in stellar IMF and DM content. This low level of intrinsic scatter cannot be ruled out by our data, although it should be noted that our sample is restricted to the most massive systems and scatter may be mass dependent. Our study of correlations involving total mass, including the MP, adds an important piece of evidence because the MP is independent of SPS stellar mass estimates and therefore can be used to break the degeneracy between the IMF and DM. Our study

shows that the MP is consistent with having *no intrinsic scatter*, within the measurement errors of a few hundredths of a dex ($\sigma_{\rm int} = 0.013 \pm 0.010$). Future studies comparing the M_*P with the MP to even higher degrees of precision will be able to quantify the contribution of IMF variations to the intrinsic scatter of the M_*P.

The tightness of scaling relations is especially remarkable in a scenario where evolution is driven by major mergers (e.g., van der Wel et al. 2009). For example, dry mergers tend to move galaxies within the FP and MP correlations and preserve their tightness. However, dry mergers do not, in general, retain the tightness of the bivariate projections of the parameter planes (Nipoti et al. 2003, 2009a; Boylan-Kolchin et al. 2006). The properties of the progenitors must be finely tuned with the orbital parameter of the merger in order to produce the tight observed scaling relations. Nipoti et al. (2009a) used these relations to show that only half of the mass in ETGs at $z = 0$ can result from dry merging and dry merging cannot cause super-massive galaxies at high redshifts (e.g., Trujillo et al. 2006; van Dokkum et al. 2008) to evolve into present-day ETGs.

6. SUMMARY

We briefly summarize the most significant conclusions from our analysis of the early-type lenses from the SLACS survey.

1. The SLACS sample obeys all the standard correlations found for non-lensing ETGs, consistent with the hypothesis that it is representative of velocity dispersion-selected ETGs.
2. Stellar kinematics and lensing data constrain the slope of the total mass-density profile ($\rho_{\rm tot} \propto r^{-\gamma'}$). The average slope is found to be close to, but slightly steeper than, isothermal, with $\langle\gamma'\rangle = 2.078 \pm 0.027$ and an intrinsic scatter of 0.16 ± 0.02.
3. The total mass-density slope γ' correlates with effective radius (r_e) and central mass density ($\Sigma_{\rm tot}$) in the sense that denser galaxies have steeper profiles. The residual intrinsic scatter is reduced but still significant (0.12 ± 0.02 for $\Sigma_{\rm tot}$).
4. Tight correlations are found between dimensional mass $M_{\rm dim} = \frac{5\sigma^2 r_e}{G}$, stellar ($M_*$) and total mass ($M_{\rm tot}$). The relationship between total mass and dimensional mass is found to be consistent with linear with very little scatter, implying that the virial coefficient of ETGs is constant over this mass range. The correlation between total (dynamical) mass and stellar mass is nonlinear ($M_* \propto M_{r_e/2}^{0.8}$), consistent with the hypothesis that the central CDM content and/or the normalization of the stellar IMF changes with mass.
5. Assuming a universal IMF the stellar mass-to-light ratio is nearly constant over the range in masses probed by the SLACS ETGs. In contrast, the total mass-to-light ratio correlates strongly with lens properties; the most significant correlations are with the central velocity dispersion and central total mass. As a result, the DM fraction within $r_e/2$ is a monotonically increasing function of galaxy mass and size. If the universal IMF assumption is relaxed, the trend could be explained at least in part by an increasing IMF normalization with galaxy mass.
6. The MP, obtained by replacing surface brightness with surface mass density in the FP, is found to be tighter and closer to the virial relation than the FP and the M_*P, indicating that the scatter of those relations is dominated by stellar populations effects.
7. We construct the FPH by adding stellar masses to the MP and find that the stellar mass coefficient is consistent with zero and there is effectively no residual intrinsic scatter.

Our results demonstrate that the dynamical structure of massive ETGs is not scale invariant and that it is fully specified by size, stellar velocity dispersion, and total mass. Although the basic trends can be explained qualitatively in terms of varying star formation efficiency as a function of halo mass and as the result of dry and wet mergers, reproducing quantitatively the observed correlations and their tightness may be a significant challenge for galaxy formation models. A more detailed modeling effort is presented in a follow-up paper, where weak-lensing data are combined with the present data to strengthen the connection between the central part of the galaxies and the virial mass of the halos in which they are embedded (Auger et al. 2010).

T.T. acknowledges support from NSF thorough CAREER award NSF-0642621, by the Sloan Foundation through a Sloan Research Fellowship and by the Packard Foundation through a Packard Fellowship. L.K. is supported through an NWO-VIDI program subsidy (project number 639.042.505). R.G. acknowledges support from the Centre National des Etudes Spatiales. The work of L.A.M. was carried out at the Jet Propulsion Laboratory, California Institute of Technology, under a contract with NASA. Support for programs 10494, 10798, and 11202 was provided by NASA through grants from the Space Telescope Science Institute. STScI is operated by the Association of Universities for Research in Astronomy, Inc., under NASA contract NAS5-26555. Support for programs 10494, 10798, and 11202 was provided by NASA through grants from the Space Telescope Science Institute. This work has made use of the SDSS database. Funding for the SDSS and SDSS-II has been provided by the Alfred P. Sloan Foundation, the Participating Institutions, the National Science Foundation, the U.S. Department of Energy, the National Aeronautics and Space Administration, the Japanese Monbukagakusho, the Max Planck Society, and the Higher Education Funding Council for England.

REFERENCES

Auger, M. W. 2008, MNRAS, 383, L40
Auger, M. W., Treu, T., Bolton, A. S., Gavazzi, R., Koopmans, L. V. E., Marshall, P. J., Bundy, K., & Moustakas, L. A. 2009, ApJ, 705, 1099
Auger, M. W., Treu, T., Gavazzi, R., Bolton, A. S., Koopmans, L. V. E., & Marshall, P. J. 2010, ApJ, 721, L163
Balogh, M. L., Baldry, I. K., Nichol, R., Miller, C., Bower, R., & Glazebrook, K. 2004, ApJ, 615, L101
Barnabè, M., Auger, M. W., Treu, T., Koopmans, L., Bolton, A. S., Czoske, O., & Gavazzi, R. 2010, MNRAS, 406, 2339
Barnabè, M., Czoske, O., Koopmans, L. V. E., Treu, T., Bolton, A. S., & Gavazzi, R. 2009, MNRAS, 399, 21
Bernardi, M., et al. 2003, AJ, 125, 1866
Bertschinger, E. 1985, ApJS, 58, 39
Bolton, A. S., Burles, S., Koopmans, L. V. E., Treu, T., Gavazzi, R., Moustakas, L. A., Wayth, R., & Schlegel, D. J. 2008a, ApJ, 682, 964
Bolton, A. S., Burles, S., Koopmans, L. V. E., Treu, T., & Moustakas, L. A. 2006, ApJ, 638, 703
Bolton, A. S., Burles, S., Treu, T., Koopmans, L. V. E., & Moustakas, L. A. 2007, ApJ, 665, L105
Bolton, A. S., Treu, T., Koopmans, L. V. E., Gavazzi, R., Moustakas, L. A., Burles, S., Schlegel, D. J., & Wayth, R. 2008b, ApJ, 684, 248
Boylan-Kolchin, M., & Ma, C.-P. 2004, MNRAS, 349, 1117
Boylan-Kolchin, M., Ma, C.-P., & Quataert, E. 2006, MNRAS, 369, 1081
Bundy, K., Treu, T., & Ellis, R. S. 2007, ApJ, 665, L5
Bundy, K., et al. 2006, ApJ, 651, 120
Cappellari, M., et al. 2006, MNRAS, 366, 1126
Cardone, V. F., & Tortora, C. 2010, MNRAS, 1471

Cardone, V. F., Tortora, C., Molinaro, R., & Salzano, V. 2009, A&A, 504, 769
Ciotti, L., Lanzoni, B., & Renzini, A. 1996, MNRAS, 282, 1
Ciotti, L., Lanzoni, B., & Volonteri, M. 2007, ApJ, 658, 65
Cooper, M. C., et al. 2006, MNRAS, 370, 198
Cowie, L. L., Songaila, A., Hu, E. M., & Cohen, J. G. 1996, AJ, 112, 839
Daddi, E., et al. 2005, ApJ, 626, 680
de Vaucouleurs, G. 1948, Ann. Astrophys., 11, 247
Dekel, A., Kowitt, M., & Shaham, J. 1981, ApJ, 250, 561
Del Popolo, A., & Kroupa, P. 2009, A&A, 502, 733
Djorgovski, S., & Davis, M. 1987, ApJ, 313, 59
Dobke, B. M., & King, L. J. 2006, A&A, 460, 647
Dressler, A. 1980, ApJ, 236, 351
Dressler, A., Lynden-Bell, D., Burstein, D., Davies, R. L., Faber, S. M., Terlevich, R., & Wegner, G. 1987, ApJ, 313, 42
Faber, S. M., Dressler, A., Davies, R. L., Burstein, D., & Lynden-Bell, D. 1987, in Nearly Normal Galaxies, From the Planck Time to the Present (New York: Springer-Verlag), 175
Faber, S. M., & Jackson, R. E. 1976, ApJ, 204, 668
Gallazzi, A., Charlot, S., Brinchmann, J., & White, S. D. M. 2006, MNRAS, 370, 1106
Gerhard, O., Kronawitter, A., Saglia, R. P., & Bender, R. 2001, AJ, 121, 1936
Gnedin, O. Y., Kravtsov, A. V., Klypin, A. A., & Nagai, D. 2004, ApJ, 616, 16
González-García, A. C., Oñorbe, J., Domínguez-Tenreiro, R., & Gómez-Flechoso, M. Á. 2009, A&A, 497, 35
Graves, G. J., & Faber, S. M. 2010, ApJ, 717, 803
Grillo, C. 2010, ApJ, 722, 779
Grillo, C., & Gobat, R. 2010, MNRAS, 402, L67
Grillo, C., Gobat, R., Lombardi, M., & Rosati, P. 2009, A&A, 501, 461
Gunn, J. E. 1977, ApJ, 218, 592
Hernquist, L. 1990, ApJ, 356, 359
Humphrey, P. J., & Buote, D. A. 2010, MNRAS, 403, 2143
Hyde, J. B., & Bernardi, M. 2009a, MNRAS, 394, 1978
Hyde, J. B., & Bernardi, M. 2009b, MNRAS, 396, 1171
Jiang, G., & Kochanek, C. S. 2007, ApJ, 671, 1568
Jorgensen, I., Franx, M., & Kjaergaard, P. 1995, MNRAS, 276, 1341
Jorgensen, I., Franx, M., & Kjaergaard, P. 1996, MNRAS, 280, 167
Kelly, B. C. 2007, ApJ, 665, 1489
Kochanek, C. S. 2006, in Saas-Fee Advanced Course 33, Gravitational Lensing: Strong, Weak and Micro, ed. G. Meylan, P. Jetzer, & P. North (Berlin: Springer), 91
Komatsu, E., et al. 2009, ApJS, 180, 330
Koopmans, L. V. E., Treu, T., Bolton, A. S., Burles, S., & Moustakas, L. A. 2006, ApJ, 649, 599
Koopmans, L. V. E., Treu, T., Fassnacht, C. D., Blandford, R. D., & Surpi, G. 2003, ApJ, 599, 70
Koopmans, L. V. E., et al. 2009, ApJ, 703, L51
Kormendy, J. 1977, ApJ, 218, 333
Kormendy, J., Fisher, D. B., Cornell, M. E., & Bender, R. 2009, ApJS, 182, 216
Lackner, C. N., & Ostriker, J. P. 2010, ApJ, 712, 88
Loeb, A., & Peebles, P. J. E. 2003, ApJ, 589, 29
Naab, T., Johansson, P. H., Ostriker, J. P., & Efstathiou, G. 2007, ApJ, 658, 710
Napolitano, N. R., Romanowsky, A. J., & Tortora, C. 2010, MNRAS, 405, 2351
Natarajan, P., Kneib, J.-P., Smail, I., Treu, T., Ellis, R., Moran, S., Limousin, M., & Czoske, O. 2009, ApJ, 693, 970
Navarro, J. F., et al. 2004, MNRAS, 349, 1039
Nipoti, C., Londrillo, P., & Ciotti, L. 2003, MNRAS, 342, 501
Nipoti, C., Treu, T., Auger, M. W., & Bolton, A. S. 2009a, ApJ, 706, L86
Nipoti, C., Treu, T., & Bolton, A. S. 2008, MNRAS, 390, 349
Nipoti, C., Treu, T., & Bolton, A. S. 2009b, ApJ, 703, 1531
Oguri, M. 2007, ApJ, 660, 1
Rettura, A., et al. 2006, A&A, 458, 717
Robertson, B., Cox, T. J., Hernquist, L., Franx, M., Hopkins, P. F., Martini, P., & Springel, V. 2006, ApJ, 641, 21
Sérsic, J. L. 1968, Atlas de Galaxies Australes (Cordoba: Observatorio Astronomico)
Shen, S., Mo, H. J., White, S. D. M., Blanton, M. R., Kauffmann, G., Voges, W., Brinkmann, J., & Csabai, I. 2003, MNRAS, 343, 978
Stockton, A., Shih, H.-Y., & Larson, K. 2010, ApJ, 709, L58
Suyu, S. H., Marshall, P. J., Auger, M. W., Hilbert, S., Blandford, R. D., Koopmans, L. V. E., Fassnacht, C. D., & Treu, T. 2010, ApJ, 711, 201
Suyu, S. H., Marshall, P. J., Hobson, M. P., & Blandford, R. D. 2006, MNRAS, 371, 983
Taylor, E. N, Franx, M., Glazebrook, K., Brinchmann, J., van der Wel, A., & van Dokkum, P. G. 2010, ApJ, 720, 723
Thomas, D., Maraston, C., Bender, R., & Mendes de Oliveira, C. 2005, ApJ, 621, 673
Tortora, C., Napolitano, N. R., Romanowsky, A. J., Capaccioli, M., & Covone, G. 2009, MNRAS, 396, 1132
Tortora, C., Napolitano, N. R., Romanowsky, A. J., & Jetzer, P. 2010, ApJ, 721, L1
Treu, T. 2010, ARA&A, 48, 87
Treu, T., Auger, M. W., Koopmans, L. V. E., Gavazzi, R., Marshall, P. J., & Bolton, A. S. 2010, ApJ, 709, 1195
Treu, T., Gavazzi, R., Gorecki, A., Marshall, P. J., Koopmans, L. V. E., Bolton, A. S., Moustakas, L. A., & Burles, S. 2009, ApJ, 690, 670
Treu, T., & Koopmans, L. V. E. 2002, MNRAS, 337, L6
Treu, T., & Koopmans, L. V. E. 2004, ApJ, 611, 739
Treu, T., Koopmans, L. V., Bolton, A. S., Burles, S., & Moustakas, L. A. 2006, ApJ, 640, 662
Treu, T., Stiavelli, M., Møller, P., Casertano, S., & Bertin, G. 2001, MNRAS, 326, 221
Trujillo, I., Cenarro, A. J., de Lorenzo-Cáceres, A., Vazdekis, A., de la Rosa, I. G., & Cava, A. 2009, ApJ, 692, L118
Trujillo, I., et al. 2006, ApJ, 650, 18
van Albada, T. S. 1982, MNRAS, 201, 939
van der Wel, A., Rix, H.-W., Holden, B. P., Bell, E. F., & Robaina, A. R. 2009, ApJ, 706, L120
van Dokkum, P. G., et al. 2008, ApJ, 677, L5
Warren, S. J., & Dye, S. 2003, ApJ, 590, 673
Wucknitz, O. 2002, MNRAS, 332, 951
York, D. G., et al. 2000, AJ, 120, 1579